pp 173–204. © Royal Aeronautical Society 2017
doi: 10.1017/aer.2017.125

Composite control system of hybrid-driven mid-altitude airship

L. Chen
chen2006@sjtu.edu.cn
School of Aeronautics and Astronautics
Shanghai Jiao Tong University
Shanghai
P.R China

Q. Dong
Functional Teaching and Research Section
Mudanjiang Medical University
Mudanjiang
P.R China

G. Zhang and D. Duan
School of Aeronautics and Astronautics
Shanghai Jiao Tong University
Shanghai
P.R China

ABSTRACT

In general, an airship is equipped with hybrid-heterogeneous actuators: the aerodynamic surfaces, the vectored propellers and the buoyant ballonets. The aerodynamic surfaces have high efficiency in attitude control at high speed. However, vectored propellers are also introduced here for attitude control under the special working condition of low airspeed. Due to the lower thrust-to-weight ratio, the composite control of hybrid-heterogeneous actuators is the primary object in controller design for an airship. In composite attitude control, first the attitude moment allocation between aerodynamic control surfaces and vectored propellers is designed according to different dynamic airspeed, to achieve the smooth motion transition from low to high airspeed, then the weighted generalised inverse (WGI) is used to design the reconfigurable actuator allocation among the homogeneous multi-actuators, where the authority of every actuator can be decided by setting the corresponding value of the weight matrix, thus the control law is unchanged under different actuator configurations. Taking the mid-altitude airship as an example, the simulations of position control, trace tracking and altitude control are provided. Simulation results demonstrate that the attitude moments allocation obtains moment distribution between the aerodynamic surfaces and the vectored propellers under different airspeeds; the reconfigurable actuator allocation achieves

Received 13 June 2017; revised 4 November 2017; accepted 7 November 2017; first published online 7 December 2017.

a good distribution and reconfiguration among homogeneous actuators, thereby enhancing the reliability of the control system.

Keywords: Hybrid-driven mid-altitude airship; composite control; attitude moment allocation; reconfigurable actuator allocation

NOMENCLATURE

c_D	drag coefficient of airship
$c_{x\delta a}$, $c_{y\delta r}$, $c_{z\delta e}$ (1/deg)	aerodynamic force coefficients of aerodynamic surfaces
c_x, c_y, c_z	aerodynamic force coefficients of airship
D (m)	distance from current position to destination
$e_i (i = 1 \cdots 6)$	weight of maximum thrust of i^{th} propeller
$f_i (i = 1 \cdots 6)$ (N)	the thrust magnitude of i^{th} propeller
$\mathbf{f} = [f_1\ f_2\ f_3\ f_4\ f_5\ f_6]^{\text{T}}$	the thrust magnitude vector
$\mathbf{F_T}$	vector of thrust and relative moment about the volume centre
$\text{F}_{T\phi}$, $\text{F}_{T\theta}$, $\text{F}_{T\psi}$ (Nm)	attitude moments taken by propellers
$k_{\theta z}$	guidance coefficient in altitude control
k_{p}, k_d, k_i	pID coefficients
l_{ref} (m)	reference length of the airship
m (kg)	airship mass
m_x, m_y, m_z	aerodynamic moment coefficients about x, y, z axes
m_{11}, m_{22}, m_{33} (kg)	added masses
m_{44}, m_{55}, m_{66}, m_{26}, m_{35} (kg·m^2)	added inertia moments
$m_{z\delta r}$, $m_{y\delta e}$, $m_{x\delta a}$ (1/deg)	moment coefficients of aerodynamic surfaces
M_ϕ, M_θ, M_ψ (Nm)	total attitude moment
$M_{\delta\text{a}}$, $M_{\delta e}$, $M_{\delta r}$ (Nm)	attitude moment taken by aerodynamic surfaces
$\mathbf{M}_\delta$	transform matrix between control surfaces and synthetic aerodynamic surfaces
I_x, I_y, I_z, I_{xy}, I_{xz}, I_{yz} (kg·m^2)	inertia of airship
p, q, r (rad/s)	angular velocities in body-fixed frame
q_∞	dynamic pressure of airflow
$\mathbf{P}$	control coefficient matrix of propellers
$\mathbf{S}$	triangular transform matrix between propellers and thrust magnitude
S_{ref} (m^2)	reference area of airship
$\mathbf{T}$	**i**ndirect control force vector
u, v, w (m/s)	linear velocities in body-fixed frame
$\mathbf{U}_\text{A}$	the aerodynamic input vector
$\mathbf{U}_\text{T}$	the propeller input vector
$\mathbf{U} = [\text{U}_\text{T}^\text{T}\text{U}_\text{A}^\text{T}]^\text{T}$	the control input vector
V_{ol} (m^3)	volume of airship
V(m/s)	airspeed of airship
V_l, V_h (m/s)	critical airspeeds in moment allocation
x, y, z (m)	positions of airship
$(x_i, y_i, z_i) (i = 1 \cdots 6)$ (m)	mounting position of i^{th} propeller in body-fixed frame
w_a	weight of aerodynamic surfaces in moment allocation

https://doi.org/10.1017/aer.2017.125 Published online by Cambridge University Press

w_p	weight of propellers in moment allocation
$w_{\|}(i = 1 \cdots 6)$	weight of thrust magnitude of i^{th} propeller in actuator allocation
$w_{\mu i}(i = 1 \cdots 6)$	weight of vectored angle of i^{th} propeller in actuator allocation
$w_{\delta i}(i = 1, 2, 3)$	weight of i^{th} control surface in actuator allocation
$\mathbf{W_1}$	weight matrix of non-stuck propellers
$\mathbf{W_2}$	weight matrix of fault propellers
$\mathbf{W}_s$	weight matrix of stuck propellers
$\mathbf{W}_\delta$	weight matrix of control surfaces
ϕ, θ, ψ (rad)	euler angles
$\delta_i(i = 1, 2, 3)(^\circ)$	deflection angle of control surface
$\delta_a(^\circ)$	deflection angle of synthetic aileron
$\delta_e(^\circ)$	deflection angle of synthetic elevator
$\delta_r(^\circ)$	deflection angle of synthetic rudder
$\mu_i(i = 1 \cdots 6)$ (rad)	vectored angle of i^{th} propeller
$\rho(\text{kg/m}^3)$	air density

1.0 INTRODUCTION

An airship has advantages over other aircraft because of large payload ability and hovering ability in the sky, so it has wide application prospect in disaster rescue and earth observation[1]. On the other hand, an airship has large response lag and is susceptible to the environment due to its large volume and low airspeed, so effective control is still the main issue in airship research.

In this article, a mid-altitude unmanned airship flying at altitude of 7000 m is proposed, as shown in Fig. 1; it is 97 m long, with a volume of 28273 m^3 and a weight of 34634 kg. For safety reasons, it is equipped with empennages of inverse Y shape and six vectored propellers with three of them located along each side. The maximum thrust of every propeller is 1960 N. Compared with the traditional configuration of two vectored propellers, these multi-vectored propellers share the total thrust together, such that the size of a single propeller is reduced and the agile manoeuvre ability is increased. The multi-vectored propellers can realise vertical take-off and landing, also achieve attitude control at any airspeed; the fault-tolerant ability is improved because of the redundant configuration.

Many researchers have conducted studies on the traditional control of an airship[2-4]. Presently, attention is centred on the composite control of stratospheric airships of multi-actuators. Liu et al[5] investigated the feasibility and stability of the equilibrium flight of the airship in a longitudinal plane equipped with ballonets and ballast. Fan et al[6] studied the altitude control system for a high-altitude airship with an auxiliary ballonet and elevator. Guo and Zhou[7] presented a design method of stratospheric airships with aircrew propeller/aerodynamic compound control system. Di et al[8] studied a method for solving the attitude control problem with aerodynamic fin and vectored propeller. Chen et al[9,] and Chen and Duan[27] analysed the nonlinear composite controller with aerodynamic control surfaces, moving masses and vectored propeller. Some other studies have focused on the composite control of finless airships with vectored thrusters, including finless airships with vectored thrusters[10], finless twin-hull airships with vectored thrusters[11], and spherical airships with two vectored thrusters[12]. Similar works have also focused on vectored-thrust underwater ships[13,14].

https://doi.org/10.1017/aer.2017.125 Published online by Cambridge University Press

Figure 1. (Colour online) Overall structure of the airship.

All of the aforementioned works focused on flight control at the working altitude based on the assumption that all actuators are in normal situation, and there is no failure in the actuators. In this paper, the airship has three aerodynamic surfaces and six vectored propellers offering 15 control degrees of freedom, so the control system is over-actuated. In the case of actuator failures, the remaining ones can be reconfigured by the control allocation without having to change the controller structure.

A control allocation system implements a function that maps the desired control forces generated by the motion controller into the commands of the different actuators. Control allocation problems can be formulated as optimisation problems, where the objective typically is to produce the specified generalised forces while minimising the use of control effort (or power) subject to actuator rate and position constraints, power constraints as well as other operational constraints. The typical methods for control allocation include direct allocation algorithm[15,16], daisy-chaining algorithm[17,18], pseudo-inverse algorithm[19,20] and mathematical programming algorithm[21,22]. Among these methods, the explicit solutions can be found and implemented efficiently only by using pseudo-inverse algorithm. And the weighted-pseudo-inverse method is further used to construct the reconfigurable system, where the weights are used to represent actuator fault status[23,24].

In this article, the hybrid control allocation scheme of multi-vectored propellers and empennages is given and the composite control system is designed. First, the attitude control moments obtained from the controller are divided into aerodynamic moments and thrust moments, then there is a further allocation of aerodynamic moments among multi-aerodynamic surfaces and allocation of thrust moment and forward thrust among multi-vectored propellers. To reallocate the actuators in case of actuator failure, a weighted pseudo-inverse-based reconfiguration strategy is developed. On the strength of the robustness of the controller, the control law remains unchanged and the weights are varied corresponding to the actuator situation: normal or failed, and thus indicating rapid reconfiguration in case of failures. According to the simulation results under different fault situations, the reconfigurable

https://doi.org/10.1017/aer.2017.125 Published online by Cambridge University Press

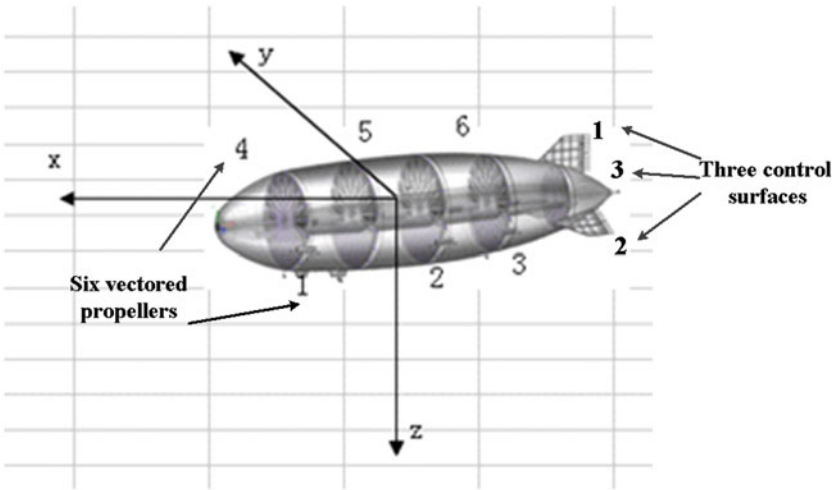

Figure 2. (Colour online) Actuator configuration of airship.

control system performs more effectively than the normal control system in cases of actuator failures, even given more than one faulty control actuator.

2.0 SYSTEM DYNAMICS

2.1 Dynamic model

The dynamic model of mid-altitude is established in the body-fixed frame. The body frame is given in Fig. 2, the position of gravity centre in body-frame is (0,0,1.898 m). The dynamics of the mid-altitude airship are similar to that of the conventional airship: external forces and moments are produced by gravity, buoyancy, fluid inertia force, aerodynamics and thrusters. Through the force analysis, the following dynamics equation can be constructed:

$$\mathbf{M}[\dot{u}_b\ \dot{v}_b\ \dot{w}_b\ \dot{p}_b\ \dot{q}_b\ \dot{r}_b]^{\mathrm{T}} = \mathbf{F_T}+\mathbf{F_{GB}}+\mathbf{F_A}+\mathbf{F_I} \quad \ldots(1)$$

$$\mathbf{M} = \begin{bmatrix} m+m_{11} & 0 & 0 & 0 & mz_G & 0 \\ 0 & m+m_{22} & 0 & -mz_G & 0 & m_{26} \\ 0 & 0 & m+m_{33} & 0 & m_{35} & 0 \\ 0 & -mz_G & 0 & I_x+m_{44} & -I_{xy} & -I_{xz} \\ mz_G & 0 & m_{53} & -I_{xy} & I_y+m_{55} & -I_{yz} \\ 0 & m_{62} & 0 & -I_{xz} & -I_{yz} & I_z+m_{66} \end{bmatrix},$$

where $\mathbf{M}$ is the mass matrix; z_G is the position of the centre of gravity; m is the mass of the airship; m_{11}, m_{22}, m_{33}, m_{44}, m_{55}, m_{66}, m_{53}, m_{62} are the added masses of the airship; I_x, I_y, I_z are the inertia moments of the airship; $\dot{u}_b$, $\dot{v}_b$, and $\dot{w}_b$ denote the linear accelerate velocities; $\dot{p}_b$, $\dot{q}_b$, and $\dot{r}_b$ denote the angular accelerate velocities about the body frame; and the right-hand side of the equation denotes the external forces and moment components in the body-fixed frame, including gravity and buoyancy $\boldsymbol{F_{GB}}$, aerodynamic control force $\boldsymbol{F_A}$, the Coriolis force $\boldsymbol{F_I}$, and vectored thrust $\boldsymbol{F_T}$ and their expressions can be found in Ref. 25. The main parameters of this airship are given in Table 1.

The aerodynamic coefficients of this airship are calculated according to computational fluid dynamics and then validated in the wind tunnel[25]. The body aerodynamic coefficients with a

https://doi.org/10.1017/aer.2017.125 Published online by Cambridge University Press

Table 1
Main parameters of an airship

Mounting position of propellers (m)	**Added mass and moments (kg) or (kg·m^2)**
$(x_1,y_1,z_1) = (27.08,-12.01,5.32)$	$m_{11} = 2.68 \times 10^3$
$(x_2,y_2,z_2) = (-4.91,-13.09, 5.96)$	$m_{22} = 2.71 \times 10^4$
$(x_3,y_3,z_3) = (-20.91,-12.01,5.32)$	$m_{33} = 2.93 \times 10^4$
$(x_4,y_4,z_4) = (27.08,12.01,5.32)$	$m_{44} = 1.37 \times 10^6$
$(x_5,y_5,z_5) = (-4.91,13.09,5.96)$	$m_{55} = 1.42 \times 10^7$, $m_{66} = 1.04 \times 10^7$
$(x_6,y_6,z_6) = (-20.91,12.01,5.32)$	$m_{26} = 6.29 \times 10^4$, $m_{35} = 1.53 \times 10^5$
Mass and inertia(kg) or (kg·m^2)	Coefficients of control surfaces (1/deg)
$m = 34{,}634$	$c_\delta = 4.4 \times 10^{-4}$
$I_x = 2.97 \times 10^6$, $I_y = 1.67 \times 10^7$, $I_z = 1.72 \times 10^7$	$m_\delta = 6.3 \times 10^{-4}$
$I_{xy} = 1.66 \times 10^1$, $I_{xz} = 6.731780 \times 10^5$, $I_{yz} = 0$	

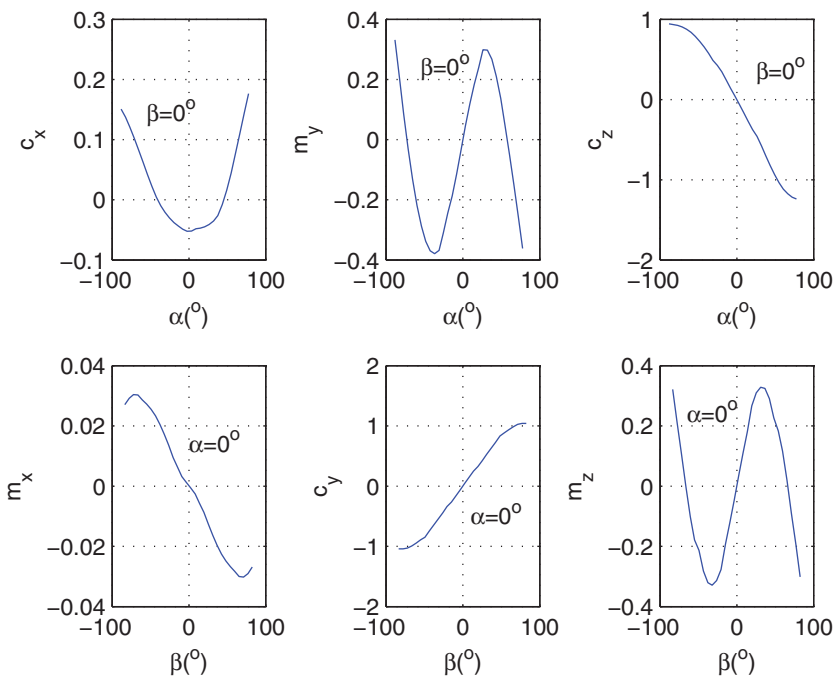

Figure 3. (Colour online) Aerodynamic coefficients of the airship body.

single-flow angle are shown in Fig. 3, where c_x, c_y, c_z are the aerodynamic force coefficients along x, y, z axes, m_x, m_y, m_z are the aerodynamic moment coefficients about x, y, z axes.

2.2 Actuator models

2.2.1 Equivalent aerodynamic model

The empennages of inverse Y shape have three independent control surfaces $\mathbf{U}_A = [\delta_1, \delta_2, \delta_3]^T$as defined in Fig. 4. The airship has three independent control surfaces δ_1, δ_2 and

https://doi.org/10.1017/aer.2017.125 Published online by Cambridge University Press

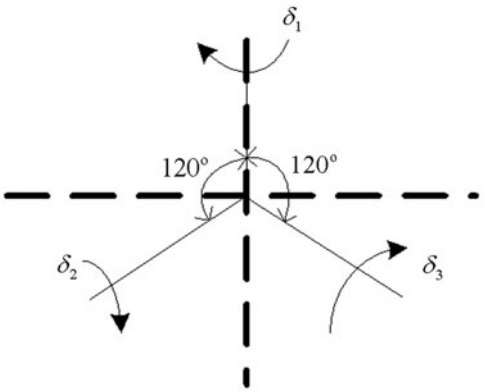

Figure 4. Control surfaces definition.

δ_3, where δ_1 is used as the rudder andδ_2 and δ_3 are used as the elevator or rudder, but they can't be used as rudder and elevator together. When they are used as the rudder, there is coupled aileron deflection. For the convenience of aerodynamics calculations, they are transformed into equivalent synthetic aerodynamic surfaces: aileron, elevator and rudder in Equation (2).

$$\begin{bmatrix} \delta_a \\ \delta_e \\ \delta_r \end{bmatrix} = \mathbf{M}_\delta \begin{bmatrix} \delta_1 \\ \delta_2 \\ \delta_3 \end{bmatrix} \quad \ldots (2)$$

$$\begin{aligned} -30^o \le \delta_i \le 30^o \\ -5^o/s \le \dot{\delta}_i \le 5^o/s \end{aligned} \quad i = 1, 2, 3,$$

here $\mathbf{M}_\delta$ is the transform matrix between control surfaces and equivalent aerodynamic surfaces:

$$\mathbf{M}_\delta = \begin{bmatrix} 0 & \frac{\sqrt{3}}{2} & \frac{\sqrt{3}}{2} \\ 0 & -\frac{\sqrt{3}}{2} & \frac{\sqrt{3}}{2} \\ -1 & \frac{1}{2} & \frac{1}{2} \end{bmatrix}$$

The aerodynamic control force $\mathbf{F_A} = [\mathbf{F}_\delta^{\mathrm{T}}, \mathbf{M}_\delta^{\mathrm{T}}]^{\mathrm{T}}$ in dynamic model (Equation (1)) are calculated according to equivalent synthetic aerodynamic surfaces:

$$\begin{aligned} \mathbf{F}_\delta &= [q_\infty S_{ref} c_{x\delta_a} \delta_a, q_\infty S_{ref} c_{y\delta_r} \delta_r, q_\infty S_{ref} c_{z\delta_e} \delta_e]^{\mathrm{T}} \\ \mathbf{M}_\delta &= [q_\infty S_{ref} l_{ref} m_{x\delta_a} \delta_a, q_\infty S_{ref} l_{ref} m_{y\delta_e} \delta_e, q_\infty S_{ref} l_{ref} m_{z\delta_r} \delta_r]^{\mathrm{T}}, \end{aligned} \quad \ldots (3)$$

where $q_\infty = 1/2\rho V^2$ is dynamic pressure of airflow, the reference surface is $S_{ref} = {V_{ol}}^{2/3}$ and reference length is $l_{ref} = {V_{ol}}^{1/3}$ (V_{ol}: airship volume).

https://doi.org/10.1017/aer.2017.125 Published online by Cambridge University Press

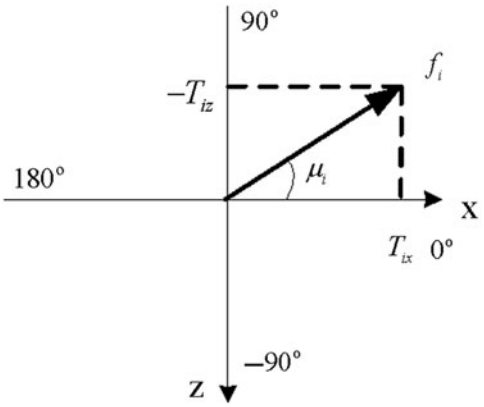

Figure 5. Vectored propeller definition.

2.2.2 Indirect control force model

Each vectored propeller can change its thrust magnitude and direction independently as shown in Fig. 5. Hence, there are twelve control variables from the vectored propellers $\mathbf{U}_\mathrm{T} = [f_1, f_2, f_3, f_4, f_5, f_6, \mu_1, \mu_2, \mu_3, \mu_4, \mu_5, \mu_6]^\mathrm{T}$, Each propeller is decoupled into two vertical components in the xoz plane of body-fixed frame,

$$\begin{aligned} T_{ix} &= f_i \cos\mu_i \\ T_{iz} &= -f_i \sin\mu_i \end{aligned} \quad \ldots(4)$$

$$\begin{aligned} &0 \le f_i \le 1960N, i = 1, \ldots, 6 \\ &-100N/s \le \dot{f}_i \le 100N/s, i = 1, \ldots, 6 \\ &-180^o \le \mu_i \le 180^o \\ &-30^o/s \le \dot{\mu}_i \le 30^o/s \end{aligned}$$

Thus, the control vectored thrust vector $\mathbf{F_T}$ in dynamic model (Equation (1)) can be described as:

$$\mathbf{F_T} = \mathbf{PT} \quad \ldots(5)$$

$$\mathbf{F_T} = [F_{Tx}, F_{Ty}, F_{Tz}, F_{T\phi}, F_{T\theta}, F_{T\psi}]^\mathrm{T}$$

$$\mathbf{T} = \begin{bmatrix} T_{1x} & T_{2x} & T_{3x} & T_{4x} & T_{5x} & T_{6x} & T_{1z} & T_{2z} & T_{3z} & T_{4z} & T_{5z} & T_{6z} \end{bmatrix}^\mathrm{T},$$

$$\mathbf{P} = \begin{bmatrix} 1 & 1 & 1 & 1 & 1 & 1 & 0 & 0 & 0 & 0 & 0 & 0 \\ 0 & 0 & 0 & 0 & 0 & 0 & 0 & 0 & 0 & 0 & 0 & 0 \\ 0 & 0 & 0 & 0 & 0 & 0 & 1 & 1 & 1 & 1 & 1 & 1 \\ 0 & 0 & 0 & 0 & 0 & 0 & y_1 & y_2 & y_3 & y_4 & y_5 & y_6 \\ z_1 & z_2 & z_3 & z_4 & z_5 & z_6 & -x_1 & -x_2 & -x_3 & -x_4 & -x_5 & -x_6 \\ -y_1 & -y_2 & -y_3 & -y_4 & -y_5 & -y_6 & 0 & 0 & 0 & 0 & 0 & 0 \end{bmatrix},$$

where $\mathbf{T}$ is the thrust components of six-vectored propellers in the xoz plane, called indirect control force vector, it is the connection between control thrust $\mathbf{F_T}$ and the control variables of each propeller (f_i, μ_i) by inverse calculation of Equation (4): $f_i = \sqrt{T_{ix}^2 + T_{iz}^2}$,

https://doi.org/10.1017/aer.2017.125 Published online by Cambridge University Press

$\mu_i = \text{atan2}(T_{ix}, -T_{iz})$; **P** is the control coefficient matrix of propellers, it is a constant coefficient matrix about mounting positions of propellers.

Here, indirect control force **T** is introduced, so the control coefficient matrix **P** is a constant matrix, the inverse of **P** always exists; thus, the pseudo-inverse-based actuator control allocation always has solution. The total input vector of this system is $\mathbf{U} = [\mathrm{U_T^T}, \mathrm{U_A^T}]^\mathrm{T}$.

Since the vectored propellers are moving in the longitudinal plane, there is no lateral force generated, so $F_{Ty} = 0$; And the vertical force F_{Tz} can be generated for vertical altitude change. In this article, the altitude is only controlled by pitch motion, so F_{Tz} is only passively generated. As shown in the composite control design, only F_{Tx} is taken into consideration for forward velocity control.

3.0 CONTROL SYSTEM DESIGN

3.1 Guidance strategy

In the path-following control, the position and attitude $[x_c, y_c, z_c, V_c, \phi_c, \theta_c, \psi_c]$ must be controlled. Here $(x_c, y_c, z_c) = RP(x_i, y_i, z_i)$ is the desired path point. For the given position tracking, the guidance strategy is:

$$D = \sqrt{(y_c - y)^2 + (x_c - x)^2}, \quad \ldots(6)$$

$$\psi_c = a\tan 2(y_c - y, x_c - x), \quad \ldots(7)$$

$$\phi_c = 0, \quad \ldots(8)$$

where D is the distance from current position to the destination point. The velocity in inertial frame is planned differently as the control objective changed; for position control, it is defined as:

$$\begin{cases} V_c = \text{def} & D > \Delta D \\ V_c = \frac{D}{\Delta D}\text{def} & D < \Delta D \end{cases}, \quad \ldots(9)$$

where def is any constant defined by user, ΔD is a specified distance from the destination point, and for path-following and altitude control, it is defined as:

$$V_c = def \quad \ldots(10)$$

The same guidance strategy is applied to the pitch angle planning for altitude control

$$\begin{cases} \theta_c = \text{def} & D_z > \Delta D_z \\ \theta_c = k_{\theta z}(z_c - z) & D_z < \Delta D_z \end{cases}, \quad \ldots(11)$$

where D_z is the value of altitude change, ΔD_z is a specified range from the destination altitude. So the nominal climbing velocity is

$$\dot{z}_c = -V_c \sin\theta_c \quad \ldots(12)$$

3.2 Basic controller design

For the safety reason, the incremental PID is chosen for controller design in real application.

https://doi.org/10.1017/aer.2017.125 Published online by Cambridge University Press

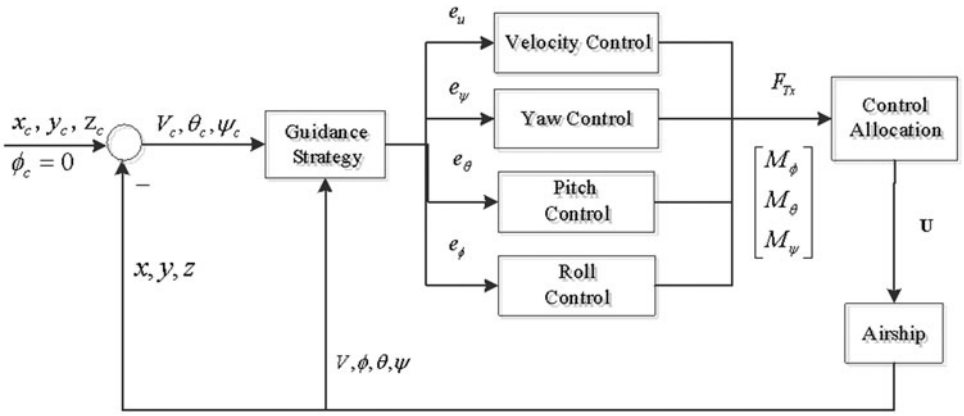

Figure 6. Basic structure of control system.

The velocity model can be approximated as a first-order inertial model, so a PI controller is adopted, where integral term is used to compensate forward aerodynamic drag.

$$\begin{aligned} e_u &= V_c - V_i \\ T_0 &= \tfrac{1}{2}\rho V_0^2 s_{\text{ref}} c_D \\ \Delta T &= k_{pu}(e_u - e_{u1}) + k_{iu} e_u \\ F_{Tx} &= T_0 + \Delta T \end{aligned} \quad \ldots(13)$$

where V_0 is the trim velocity, V_i is the current ground speed, and e_{u1} is the tracking error of last control period. The pitch motion can be approximated as a two-order oscillation model, so a PID controller is adopted, the same controller structure is designed for the roll motion to keep roll angle to zero, though there is a stabilising moment from the gravity:

$$\begin{aligned} e_\theta &= \theta_c - \theta \\ \Delta M_\theta &= k_{p\theta}(e_\theta - e_{\theta 1}) + k_{d\theta}(e_\theta - 2e_{\theta 1} + e_{\theta 2}) + k_{i\theta} e_\theta, \\ M_\theta &= M_{\theta 0} + \Delta M_\theta \end{aligned} \quad \ldots(14)$$

$$\begin{aligned} e_\phi &= \phi_c - \phi \\ \Delta M_\phi &= k_{p\phi}(e_\phi - e_{\phi 1}) + k_{d\phi}(e_\phi - 2e_{\phi 1} + e_{\phi 2}) + k_{i\phi} e_\phi \\ M_\phi &= M_{\phi 0} + \Delta M_\phi \end{aligned} \quad \ldots(15)$$

The yaw motion can be approximated as a two-order integral system, so a PD controller is used:

$$\begin{aligned} e_\psi &= \psi_c - \psi \\ \Delta M_\psi &= k_{p\psi}(e_\psi - e_{\psi 1}) + k_{d\psi}(e_\psi - 2e_{\psi 1} + e_{\psi 2}), \\ M_\psi &= M_{\psi 0} + \Delta M_\psi \end{aligned} \quad \ldots(16)$$

where $M_{\theta 0}$, $M_{\phi 0}$ and $M_{\psi 0}$ are control moments of last control period.

The overall control system structure is shown in Fig. 6. The control allocation model, which will be discussed in next two sections, includes attitude moment allocation and actuator reconfigurable allocation.

https://doi.org/10.1017/aer.2017.125 Published online by Cambridge University Press

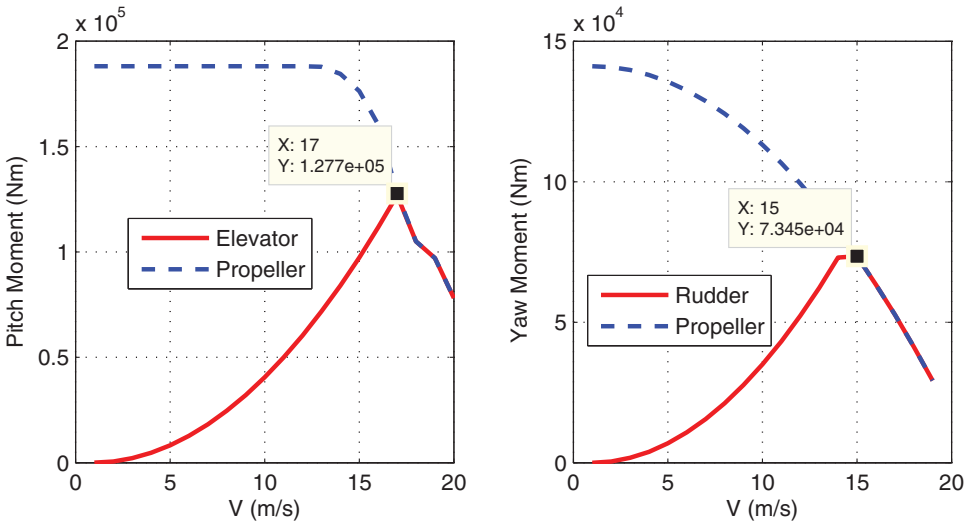

Figure 7. (Colour online) Maximum moment comparison between propellers and aerodynamic surfaces.

3.3 Attitude moment allocation

As mentioned before, both the aerodynamic surfaces and the vectored propellers can generate the attitude control moments. The attitude moments generated from the aerodynamic surfaces are affected by dynamic pressure. For an airship, the steady forward airspeed is slow, especially when hovering at fixed point, the airship's response to aerodynamic surface is slow[26]. However, propellers are less affected by airspeed and airship's response is fast under the action of vectored propellers[26]. Therefore, for the attitude moment allocation, the aerodynamic surfaces have high authority over the vectored propellers at high airspeed in consideration of energy consumption; the vectored propellers have high authority at low airspeed in consideration of manoeuverability[8,26]. Such a control allocation strategy of attitude moments between the aerodynamic surfaces and the vectored propellers can be deduced according to different airspeed,

$$\begin{cases} w_{\mathrm{a}} = (V - V_l)/(V_h - V_l),\ w_p = 1 - w_a,\ V_l < V < V_h \\ w_p = 0,\ w_a = 1,\ V \geq V_h \\ w_p = 1,\ w_a = 0,\ V \leq V_l \end{cases}, \qquad \ldots (17)$$

where w_a and w_p are weights of aerodynamic moment and thrust moment, respectively, V_h and V_l are two critical airspeeds for weight calculation. Here, the two critical airspeeds are determined by the evaluation of maximum moment outputs for a given airspeed, where the airspeed is kept by the propellers; the remaining thrust is used for pitch or yaw motion. The maximum attitude moments are compared between the propellers and aerodynamic surfaces in Fig. 7. The maximum thrust output of every propeller is 1960 N, the equivalent maximum aerodynamic deflections $\delta_{e\max} = \frac{\sqrt{3}}{2}|\delta_{2\max}| + \frac{\sqrt{3}}{2}|\delta_{3\max}| \approx 52^\circ$ and $\delta_{r\max} = |\delta_{1\max}| + \frac{1}{2}|\delta_{2\max}| + \frac{1}{2}|\delta_{3\max}| = 60^\circ$ are deduced from Equation (2). The maximum aerodynamic moments calculated from Equation (3) increase as the airspeed increases; however, the maximum thrust moments calculated from Equation (5) decrease as the airspeed

https://doi.org/10.1017/aer.2017.125 Published online by Cambridge University Press

increases; It can be seen, that the aerodynamic moment generated is comparable to that of propellers at speed of 17 m/s in pitch and 15 m/s in yaw, respectively.

For this airship, the maximum airspeed is 15 m/s, such V_h= 15m/s and V_l= 0m/s are chosen in Equation (17), it means that the vectored propellers and aerodynamic surfaces participate in attitude control in the whole airspeed range.

The attitude control moments M_ϕ, M_θ and M_ψ are obtained from controller Equations (14)-(16). Then they are divided into aerodynamic moments $\mathbf{M}_a = [M_{\delta a}, M_{\delta e}, M_{\delta r}]^{\mathrm{T}}$ and thrust moments $\mathbf{M_T} = [F_{T\phi}, F_{T\theta}, F_{T\psi}]^{\mathrm{T}}$ by integrated weight matrix.

$$\mathbf{M} = \begin{bmatrix} \mathbf{M_a} \\ \mathbf{M_T} \end{bmatrix} = \begin{bmatrix} M_{\delta a} \\ M_{\delta e} \\ M_{\delta r} \\ F_{T\phi} \\ F_{T\theta} \\ F_{T\psi} \end{bmatrix} = \begin{bmatrix} \mathrm{diag}[w_a, w_a, w_a] \\ \mathrm{diag}[w_p, w_p, w_p] \end{bmatrix} \begin{bmatrix} M_\phi \\ M_\theta \\ M_\psi \end{bmatrix} \quad \ldots(18)$$

3.4 Reconfigurable actuator allocation

After the attitude moments allocation, there is a further actuator allocation of aerodynamic moments among multi-aerodynamic surfaces and allocation of thrust moments and forward thrust among multi-vectored propellers. The actuator control allocation system is designed based on weighted pseudo-inverse method. The weights taken here are indicating the actuator's working states: normal or failed. The reconfigurable control system can reallocate the actuators simply by modifying their individual weights; thus, system reconfiguration is quick. This system is also easy to implement due to the analytic solution of allocation based on pseudo-inverse.

3.4.1 Reconfigurable allocation among multi-surfaces

Given the aerodynamic moments, the deflection angles of synthetic aerodynamic surfaces can be obtained from the dynamic model in Equation (3), then the independent control surfaces are deduced from the inverse transform of Equation (2). The weight matrix of three control surfaces is: $\mathbf{W}_\delta = \mathrm{diag}[w_{\delta 1}, w_{\delta 2}, w_{\delta 3}]$, $w_{\delta i} (i = 1, 2, 3)$ is the weight in which 1 represents normal deflection and 0 represents stuck at any initial deflection angle. After the attitude control, the fault detection will give the weight matrix. Then, the pseudo-inverse is implemented to realise actuator reconfiguration.

$$\begin{bmatrix} \delta_1 \\ \delta_2 \\ \delta_3 \end{bmatrix} = \mathrm{pinv}\,(\mathbf{M}_\delta \cdot \mathbf{W}_\delta) \begin{bmatrix} \delta_a \\ \delta_e \\ \delta_r \end{bmatrix} \quad \ldots(19)$$

3.4.2 Reconfigurable allocation among multi-propellers

For the general implementation of the propeller allocation, three diagonal weight matrices are adopted. Three kinds of weights are combined together to represent the all possible faults of vectored propeller: magnitude deficiency, vectored angle stuck and actuator failed.

The first weight matrix is $\mathbf{W_1}$, which denotes the state of every non-stuck propeller. As a result, Equation (5) is expanded to:

$$\mathbf{F_T} = \mathbf{P W_1 T}, \quad \ldots(20)$$

https://doi.org/10.1017/aer.2017.125 Published online by Cambridge University Press

where $\mathbf{W}_1 = \text{diag}[e_1 w_{\text{f1}}\ e_2 w_{\text{f2}}\ e_3 w_{\text{f3}}\ e_4 w_{\text{f4}}\ e_5 w_{\text{f5}}\ e_6 w_{\text{f6}}\ e_1 w_{\text{f1}}\ e_2 w_{\text{f2}}\ e_3 w_{\text{f3}}\ e_4 w_{\text{f4}}\ e_5 w_{\text{f5}}\ e_6 w_{\text{f6}}]$, and w_{fi} is propeller weight; and $w_{\text{fi}} = 1$ is the weight of the non-stuck actuator. If $w_{\text{fi}} = 0$, the actuator encounters fault one and may either be stuck in a vectored angle or total failed. e_i is the weight of maximum thrust of each deficient propeller.

$$F_{Timaxf} = e_i \cdot F_{Ti\max}, \quad \ldots(21)$$

where $F_{Ti\max}$ is the maximum magnitude of every normal propeller; and F_{Timaxf} is the real maximum thrust under thrust deficiency.

In a stuck fault, the trigonometric function matrix of a vectored angle must be separated with propeller magnitude. Thus, Equation (5) is rewritten again as

$$\mathbf{F_T} = \mathbf{PSf} \quad \ldots(22)$$

where f is the magnitude of single thrust output and S is the triangular transform matrix.

$$\mathbf{f} = \begin{bmatrix} f_1 & f_2 & f_3 & f_4 & f_5 & f_6 \end{bmatrix}^{\text{T}}$$
$$\mathbf{S} = [diag\ [\sin\mu_{10}\ \ \sin\mu_{20}\ \ \sin\mu_{30}\ \ \sin\mu_{40}\ \ \sin\mu_{50}\ \ \sin\mu_{60}]\ ;\ ,$$
$$diag[-\cos\mu_{10}, -\cos\mu_{20}, -\cos\mu_{30}, -\cos\mu_{40}, -\cos\mu_{50}, -\cos\mu_{60}]]$$

where μ_{i0} denotes the position at which the propeller is stuck.

In failure cases, the last two weight matrices are incorporated into Equation (22) as

$$\mathbf{F_T} = \mathbf{PW_sSW_2f}, \quad \ldots(23)$$

where $\mathbf{W}_2 = \text{diag}[e_1(1 - w_{\text{f1}})\, e_2(1 - w_{\text{f2}})\, e_3(1 - w_{\text{f3}})\, e_4(1 - w_{\text{f4}})\, e_5(1 - w_{\text{f5}})\, e_6(1 - w_{\text{f6}})]$ indicates the weight of the propeller as a result of any failure, $\mathbf{W}_s = \text{diag}[w_{\mu 1}\ w_{\mu 2}\ w_{\mu 3}\ w_{\mu 4}\ w_{\mu 5}\ w_{\mu 6}\ w_{\mu 1}\ w_{\mu 2}\ w_{\mu 3}\ w_{\mu 4}\ w_{\mu 5}\ w_{\mu 6}]$ denotes the weight of a stuck propeller, and $w_{\mu i}$ is the weight of the vectored angle. If $w_{\text{fi}} = 0$ and $w_{\mu i} = 1$, the failure is stuck at a certain vectored angle, but with the thrust magnitude. If $w_{\text{fi}} = 0$ and $w_{\mu i} = 0$, the propeller has failed completely and no action can be taken.

Thus, the total thrust force can be determined by:

$$\mathbf{F_T} = \mathbf{PW_1T} + \mathbf{PW_sSW_2f} \quad \ldots(24)$$

The first item on the right side of the Equation (24) represents the contribution of non-stuck propellers, and the second item indicates the contribution of the failed propellers. By using the weight matrix $\mathbf{W_1}$, the propeller deficiency can be considered. By introducing the weight matrixes $\mathbf{W}_s$ and $\mathbf{W}_2$, the propeller stuck can be considered. By using the weight matrixes $\mathbf{W_1}$, $\mathbf{W}_2$ and $\mathbf{W}_s$ together, the failed propeller can be considered. In this controller, the indirect control force $\mathbf{T}$ in Equation (24) is maintained, which guarantees the existence of the pseudo-inverse of constant matrixes $\mathbf{PW_1}$ and $\mathbf{PW_sSW_2}$ as long as the fault situations were given. So there always exists solution to the controller. Table 2 shows the relationship of actuator failure with the weights.

The reconfigurable actuator allocation structure is shown in Fig. 8. The redistributed pseudo-inverse technique is taken between the normal actuators and the actuators of any failure where $\mathbf{T}'$ is the **i**ndirect control force vector taken by the non-stuck propellers, $\mathbf{T}''$ is

https://doi.org/10.1017/aer.2017.125 Published online by Cambridge University Press

Table 2
Actuator state and weights

Actuator state	Propeller *i* normal	Propeller *i* failed	Propeller *i* stuck	Propeller *i* with thrust deficiency	Propeller *i* stuck and with deficiency
Weights	$w_{\mathrm{fi}} = 1$ $w_{\mu i} = 0$ $e_i = 1$	$w_{\mathrm{fi}} = 0$ $w_{\mu i} = 0$ $e_i = 0$	$w_{\mathrm{fi}} = 0$ $w_{\mu i} = 1$ $e_i = 1$	$w_{\mathrm{fi}} = 1$ $w_{\mu i} = 0$ $e_i = c < 1$	$w_{\mathrm{fi}} = 0$ $w_{\mu i} = 1$ $e_i = c < 1$

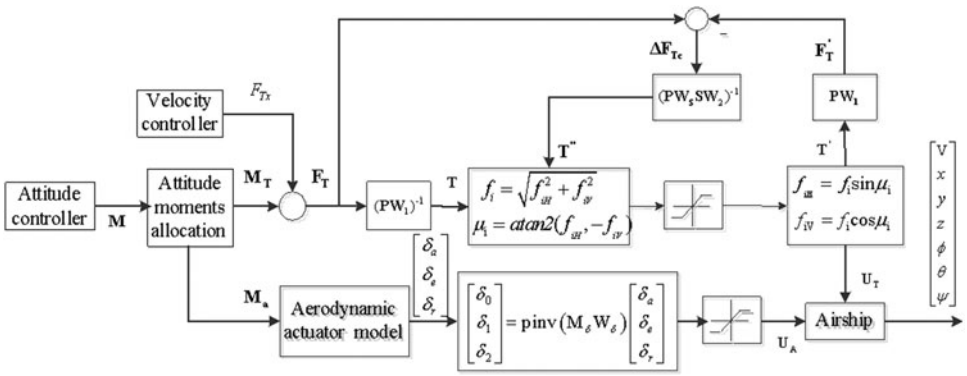

Figure 8. Reconfigurable actuator allocation structure.

the **i**ndirect control force vector taken by stuck propellers. $\mathbf{\Delta F_{Tc}}$ is the moment difference of desired moment with the moment of non-stuck propellers and it will be compensated by other faulty actuators as long as the control ability is guaranteed. In the control allocation, the non-stuck actuators have the priority to the fault actuator in actuation to achieve better performance and less energy consumption. If the commanded force cannot be satisfied, the reconfigurable controller takes effect by changing its weights to adaptation the failure of fault actuators, then reallocates residual force $\mathbf{\Delta F_{Tc}}$ among the fault actuators, and induces compensation force $\mathbf{T}''$. The fault detection model is not designed in this article, so the failures are defined in advance. The system retains full controllability as long as remaining actuators still have the actuation ability.

4.0 COMPOSITE CONTROL SIMULATION

In this section, position control, trace tracking and altitude control are implemented to validate the proposed strategies. The attitude moment allocation is achieved under different speeds and the reconfigurable actuator allocation is conducted under different actuator faults.

4.1 Control moment allocation under different airspeeds

Simulation results of composite control in normal actuator situation are shown in Figs 9-12 for position control, Figs 13-16 for trace tracking and Figs 17-20 for altitude control, respectively. And it is conducted under different trim airspeeds: $u_0 = 4\,\mathrm{m/s}$, $u_0 = 8\,\mathrm{m/s}$

https://doi.org/10.1017/aer.2017.125 Published online by Cambridge University Press

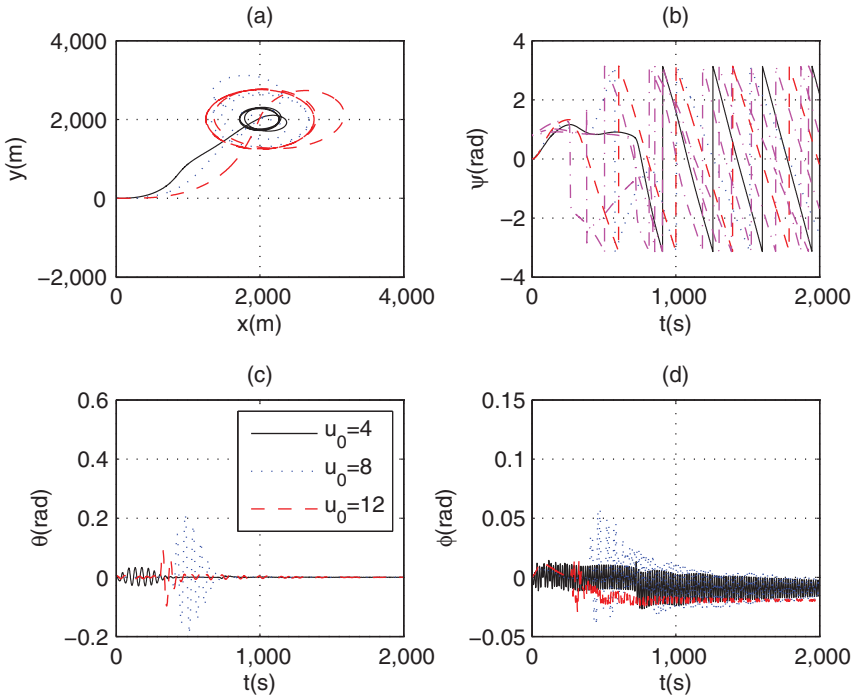

Figure 9. (Colour online) States in position control of normal cases.

and $u_0 = 12\,m/s$. Figs 10-12 show the actuator outputs for position control, Figs 14-16 show the actuator outputs for trace tracking, and Figs 18-20 show the actuator outputs of altitude control. The moment allocation weights of aerodynamic surfaces are shown in Figs 10, 14 and 18, respectively. From simulation results we can see, the attitude moment allocation strategy can regulate moment allocation weights in different airspeeds. The responses of composite control are smooth under different airspeeds, the output of every actuator is limited in its hard constrains.

In position tracking, with increasing of airspeed, the diameter of hover circle increases (Fig. 9(a)); the thrusts required also increase (Fig. 12(a)); the aerodynamic deflections decrease (Fig. 10(a)), at low airspeed, $u_0 = 4\,m/s$, the rudder reaches full position for heading control. The attitude allocation weights are varied with variation of airspeed (Fig. 10(f)).

In trajectory tracking, the tracking traces do not have much difference, with increasing of the airspeed, the aerodynamic deflections decrease (Fig. 14), the thrusts required increase (Fig. 16), The attitude allocation weights are almost unchanged with variation of airspeed (Fig. 14(f)).

In altitude control, the pitch angle is consistent with altitude change (Fig. 17), the maximum pitch angel is limited by defined constant value in guidance algorithm of Equation (11). The climbing velocity increases with the increasing of airspeed, so the climbing time is shorten with high airspeed (Fig. 17(d)). Elevator deflection increases as the airspeed decreases (Fig. 18), such that, at high speed, the difference of thrust between climbing and cruising is small (Fig. 20); the attitude allocation weights are almost unchanged with the variation of airspeed in the steady climbing and final cruising phases as long as the airspeed is stable (Fig. 18(f)).

https://doi.org/10.1017/aer.2017.125 Published online by Cambridge University Press

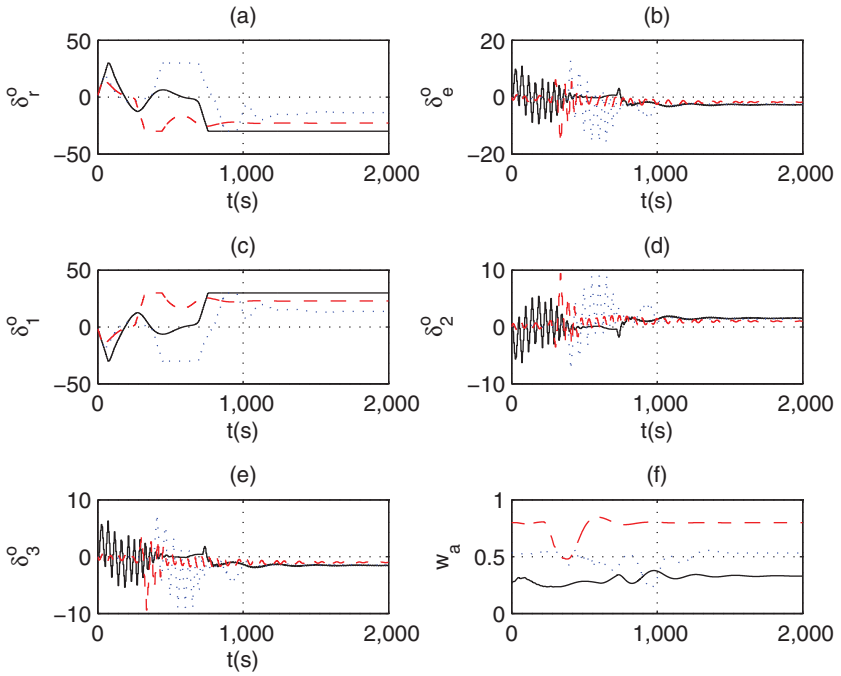

Figure 10. (Colour online) Control surfaces and moment allocation weights in position control of normal cases.

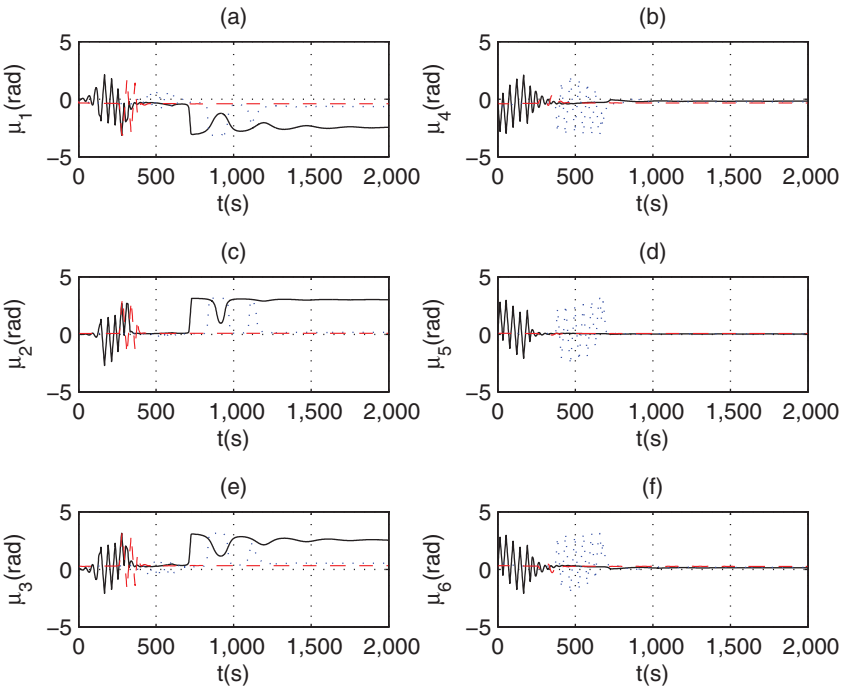

Figure 11. (Colour online) Vectored angles in position control of normal cases.

https://doi.org/10.1017/aer.2017.125 Published online by Cambridge University Press

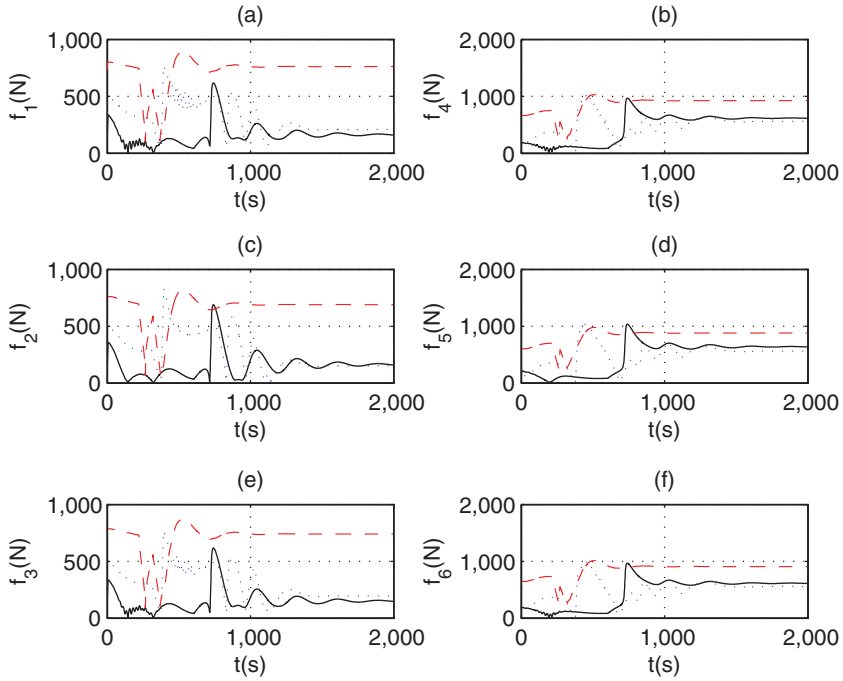

Figure 12. (Colour online) Thrusts in position control of normal cases.

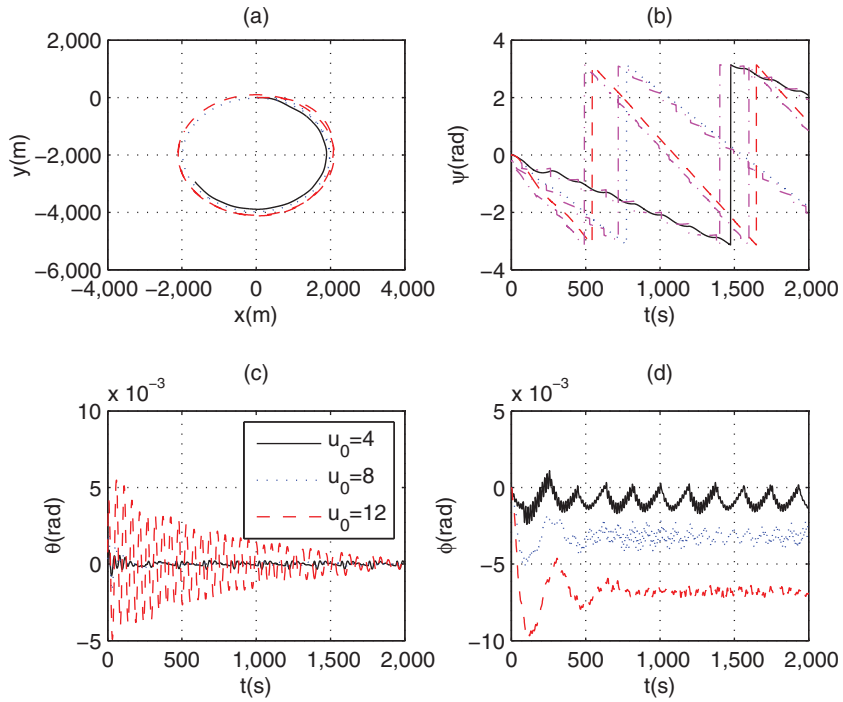

Figure 13. (Colour online) States in trace tracking of normal cases.

https://doi.org/10.1017/aer.2017.125 Published online by Cambridge University Press

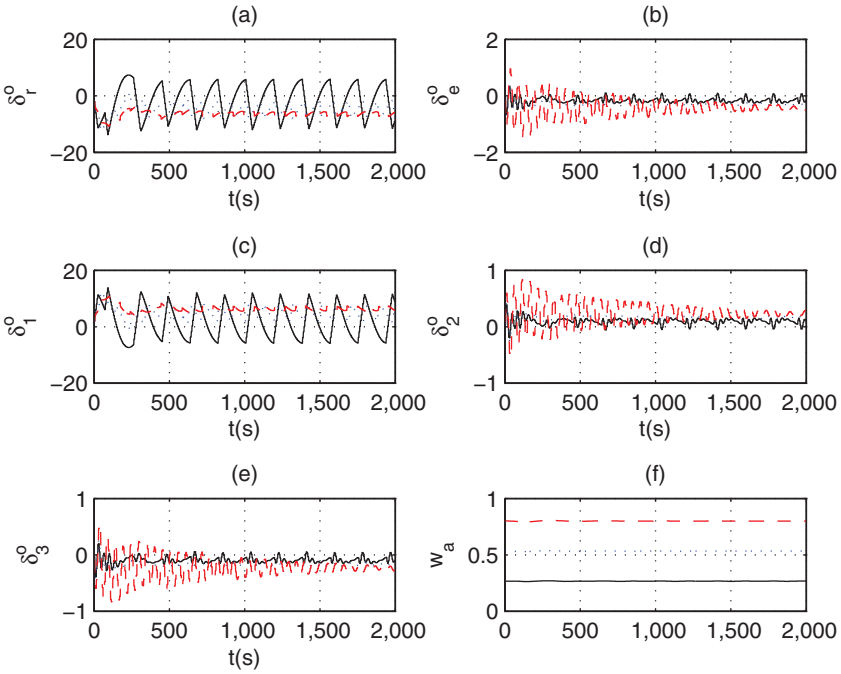

Figure 14. (Colour online) Control surfaces and moment allocation weights in trace tracking of normal cases.

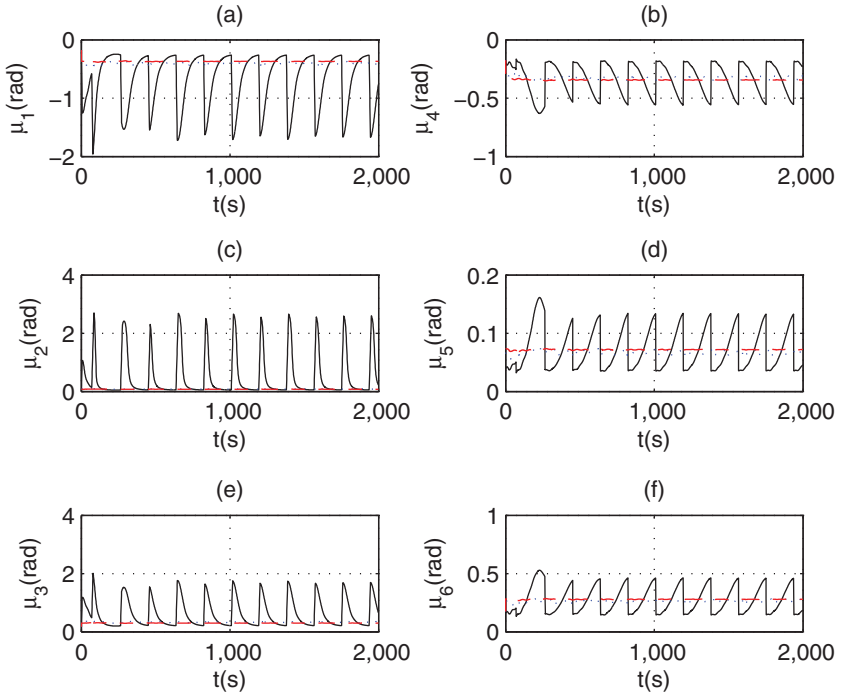

Figure 15. (Colour online) Vectored angles in trace tracking of normal cases.

https://doi.org/10.1017/aer.2017.125 Published online by Cambridge University Press

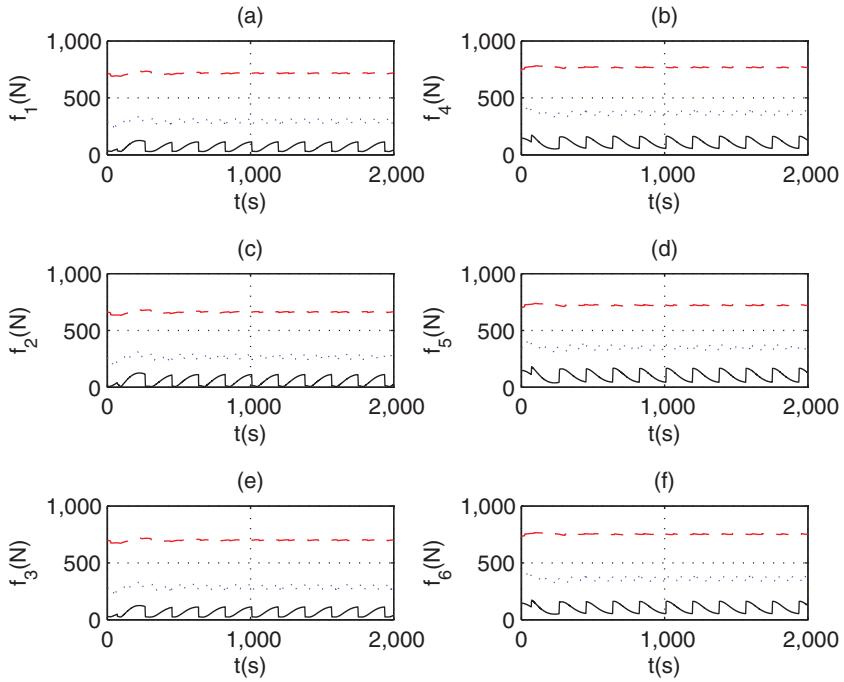

Figure 16. (Colour online) Thrusts in trace tracking of normal cases.

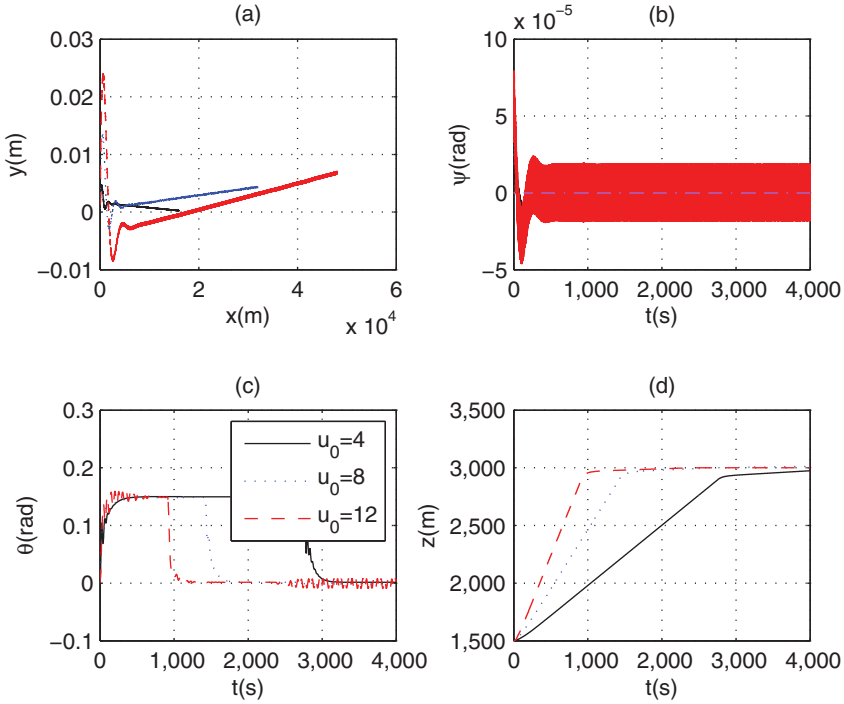

Figure 17. (Colour online) States in altitude control of normal cases.

https://doi.org/10.1017/aer.2017.125 Published online by Cambridge University Press

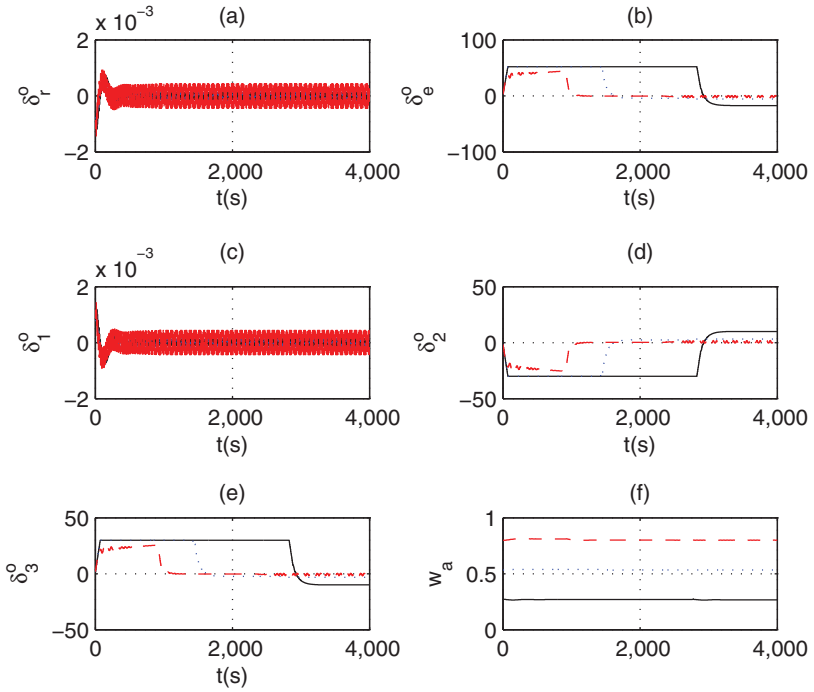

Figure 18. (Colour online) Control surfaces and moment allocation weights in altitude control of normal cases.

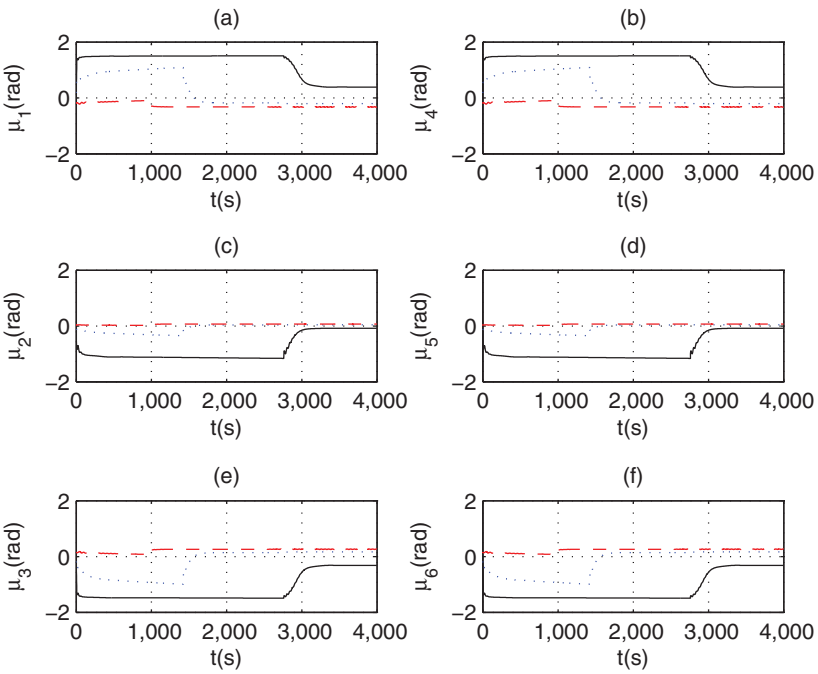

Figure 19. (Colour online) Vectored angles in altitude control of normal cases.

https://doi.org/10.1017/aer.2017.125 Published online by Cambridge University Press

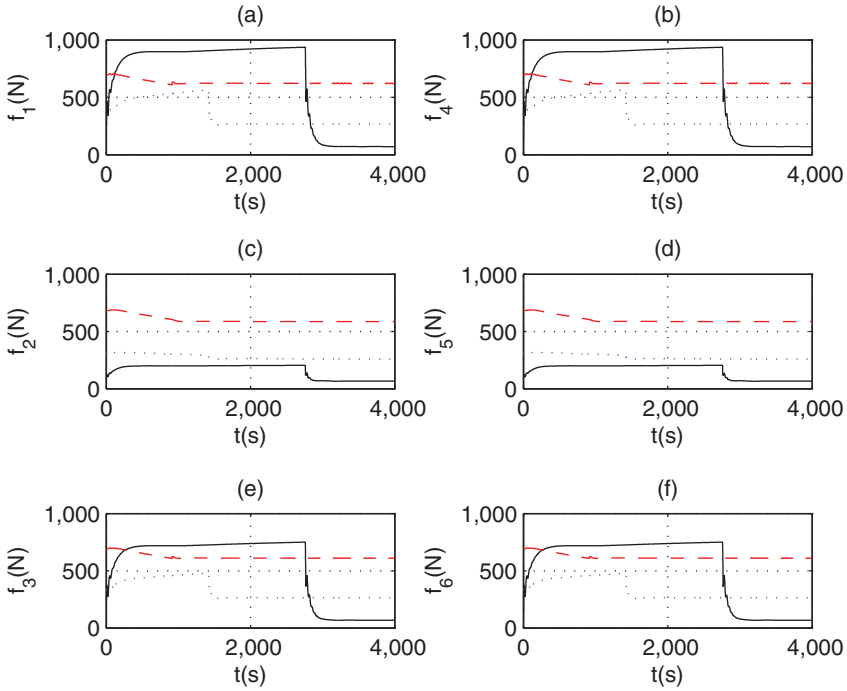

Figure 20. (Colour online) Thrusts in altitude control of normal cases.

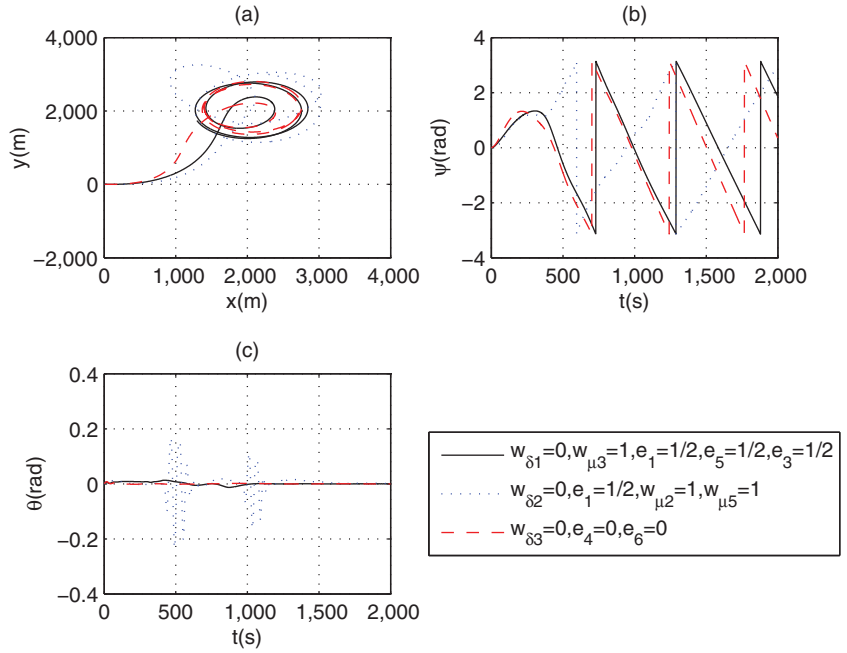

Figure 21. (Colour online) States in position control of failure cases.

https://doi.org/10.1017/aer.2017.125 Published online by Cambridge University Press

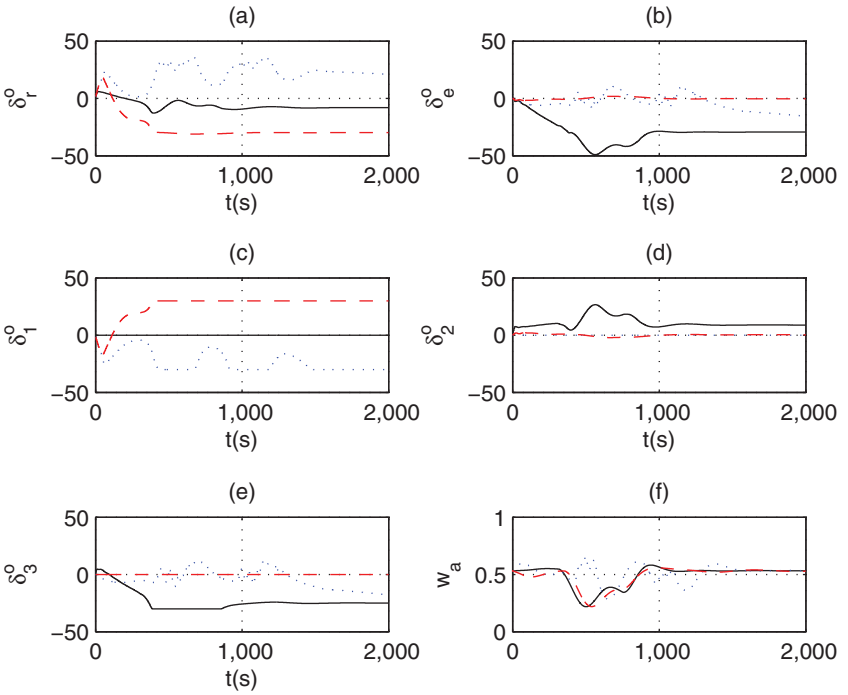

Figure 22. (Colour online) Control surfaces and moment allocation weights in position control of failure cases.

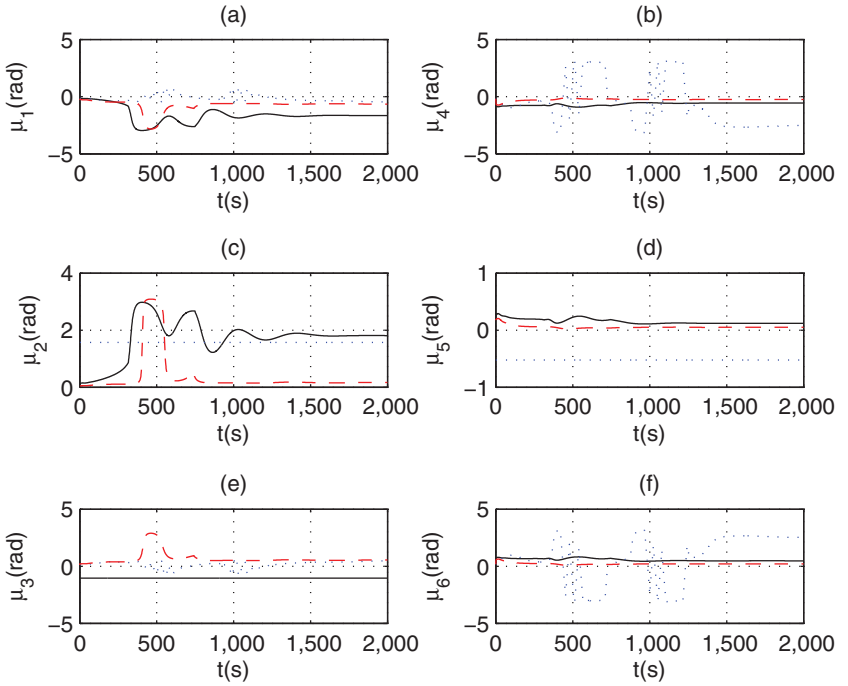

Figure 23. (Colour online) Vectored angles in position control of failure cases.

https://doi.org/10.1017/aer.2017.125 Published online by Cambridge University Press

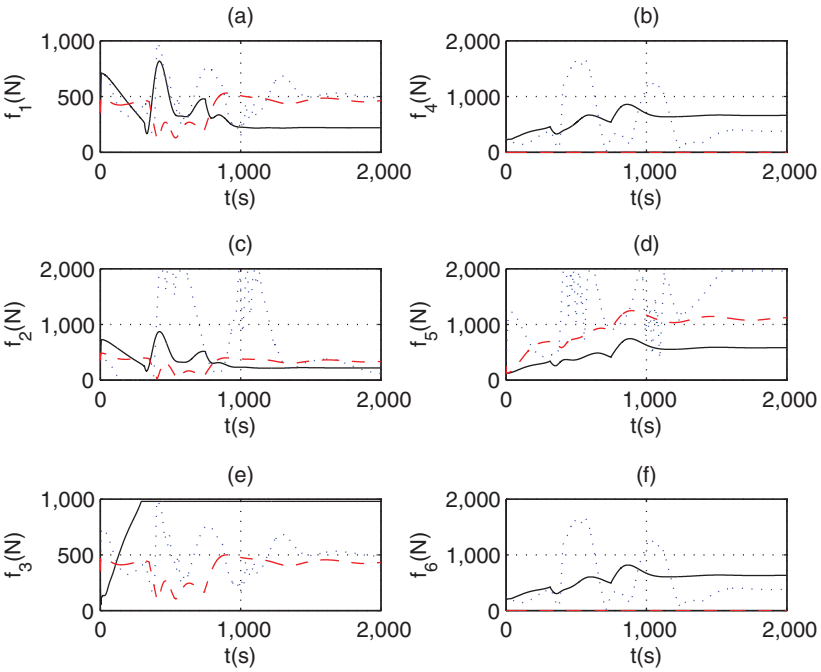

Figure 24. (Colour online) Thrusts in position control of failure cases.

4.2 Reconfigurable actuator allocation under different faults

For a given airspeed, simulation results of composite control under actuator failure cases are shown in Figs 21, 26 and 31 for position control, trace tracking and altitude control, respectively. The trim airspeed is $V_0 = 8\,\mathrm{m/s}$. And it is conducted under three different failure cases. In the first case, the fault weights are $[w_{\delta 1} = 0, w_{\mu 3} = 1, e_1 = 1/2, e_3 = 1/2, e_5 = 1/2]$, it means that the control surface 1 and propeller 3 are stuck, propellers 1,3, and 5 have a thrust deficiency of 1/2; In the second failure case, the fault weights are $[w_{\delta 2} = 0, w_{\mu 2} = 1, w_{\mu 5} = 1, e_1 = 1/2]$, which means that control surface 2 and propellers 2 and 5 are stuck, and propeller 1 has a thrust deficiency of 1/2. In the third case, the fault weights are $[w_{\delta 3} = 0, e_4 = 0, e_6 = 0]$, it means that control surface 3 is stuck and propellers 4 and 6 are totally failed. The stuck positions of all fault actuators are $\mu_{20} = 90^o$, $\mu_{30} = -60^o$, $\mu_{50} = -30^o$ and δ_{10}=0°, δ_{20}=0°, δ_{30}=0°. Figures 22-24 show the actuator outputs for position control, Figs 27-29 show the actuator outputs for trace tracking, and Figs 32-34 show the actuator outputs of altitude control. The moment allocation weights of aerodynamic surfaces are shown in Figs 22(f), 27(f) and 32(f), respectively. Figures 25, 30 and 35 give the control force allocation of multi-propellers in body-fixed frame under different actuator configurations. From the simulation results we can see, the reconfigurable actuator allocation strategy can reallocate the actuator in case of failures. The responses of composite control are smooth under different failures, the output of every actuator is limited in its hard constrains.

4.2.1 Compensation among multi-actuators

Position-tracking results in the normal case (in Fig. 9) compared with that in failure cases (in Fig. 21), there are not much differences in tracking processes. In the first failure case, propeller

https://doi.org/10.1017/aer.2017.125 Published online by Cambridge University Press

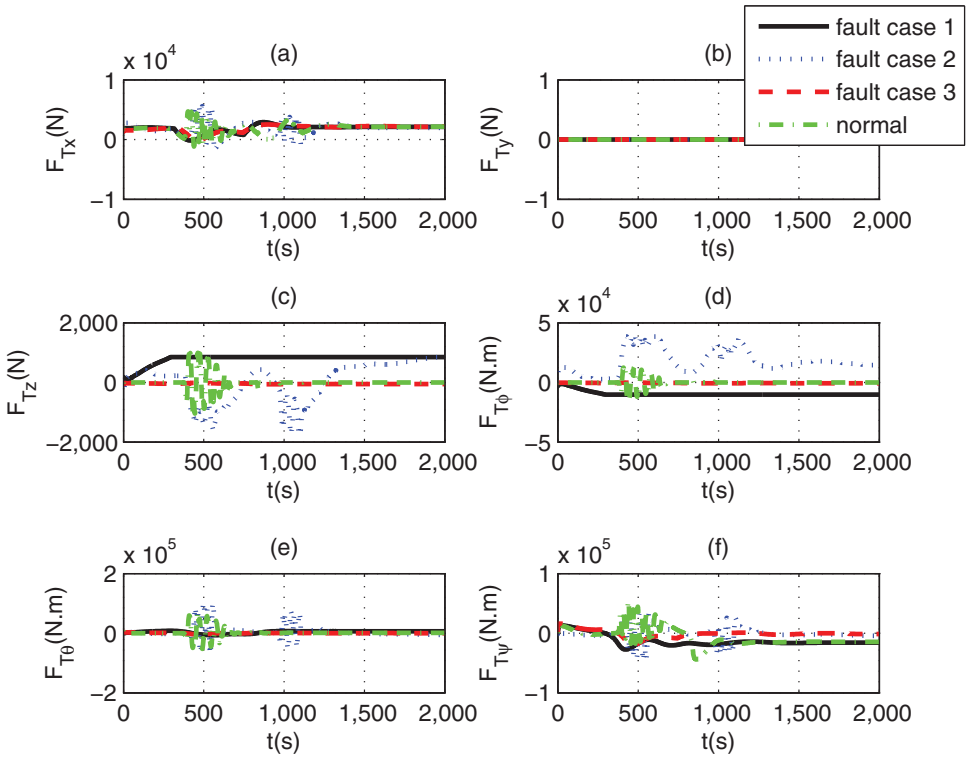

Figure 25. (Colour online) Control force allocation of propellers in position control.

3 is stuck at $\mu_{30} = -60^{o}$ and with a thrust deficiency of 1/2, so it is easy to reach its saturation position as shown in Fig. 24(e); the same situation also occurred in the second failure case in Fig. 29(e). The actuators are automatically allocated to compensate the deficiency of other actuators, for example, in Fig. 22(a), the rudder has opposite outputs in the second and third failure cases to adapt the different fault situations of propellers.

Trace-tracking results in the normal case (in Fig. 13) are compared with those in the failure cases (in Fig. 26). The final tracking results are similar, however with different actuator allocation results: for example, in the first failure case, propellers 1 and 5 are used for pitch control. Because of thrust deficiency, their pitch ability decreased, however, the elevator is used to compensate the pitch moment, as shown in Fig. 27(b); in the second failure case, the output of propeller 2 is very small (Fig. 29(c)). because it is stuck at 90° position. Its output is a disturbance for planar motion, so it should be suppressed; such the thrust output of propeller 5 is small too, because of the symmetric installation of propellers 2 and 5 (in Fig. 29(d)).

Altitude-tracking results in normal case (in Fig. 17) are compared with those in failure cases (in Fig. 30). In the second failure case, the fault propellers 1 and 5 are stuck at a certain angle, thus causing yaw disturbance. As a result, the rudder deflects at a certain angle (in Fig. 32(a)) in order to resist the yaw deviation, as shown in Fig. 31(b); and propeller 2 is stuck at 90°, so it reaches the maximum position to assist altitude control directly as shown in Fig. 34(c). For the third failure case, propellers 4 and 6 have totally failed, so only propeller 5 is used to balance the yaw moment, as shown in Fig. 34(d).

https://doi.org/10.1017/aer.2017.125 Published online by Cambridge University Press

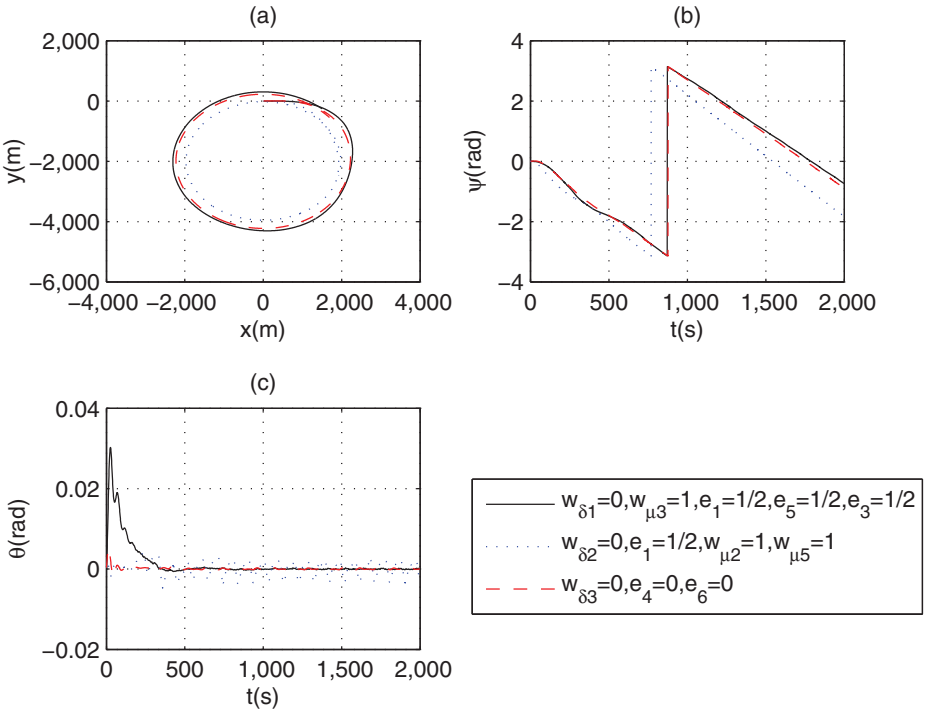

Figure 26. (Colour online) States in trace tracking of failure cases.

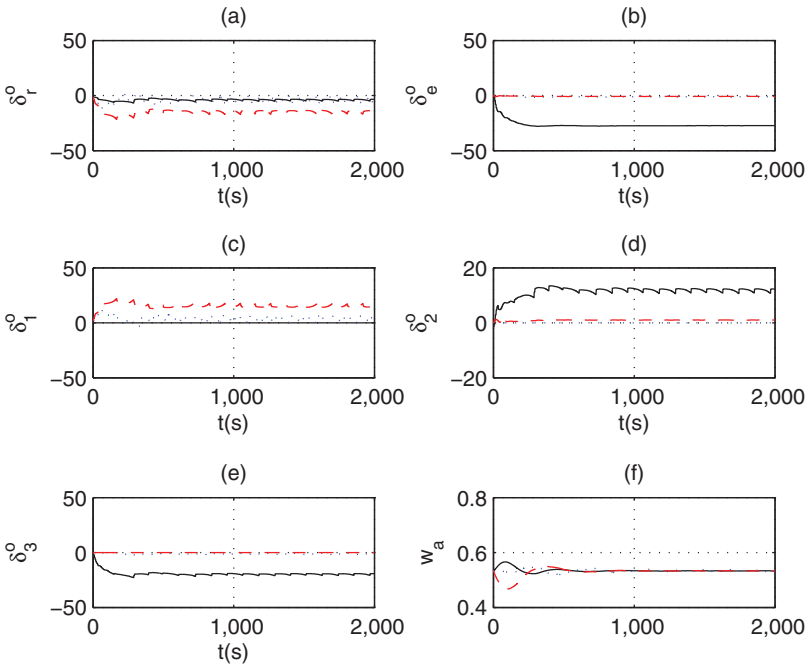

Figure 27. (Colour online) Aerodynamic deflections in trace tracking of failure cases.

https://doi.org/10.1017/aer.2017.125 Published online by Cambridge University Press

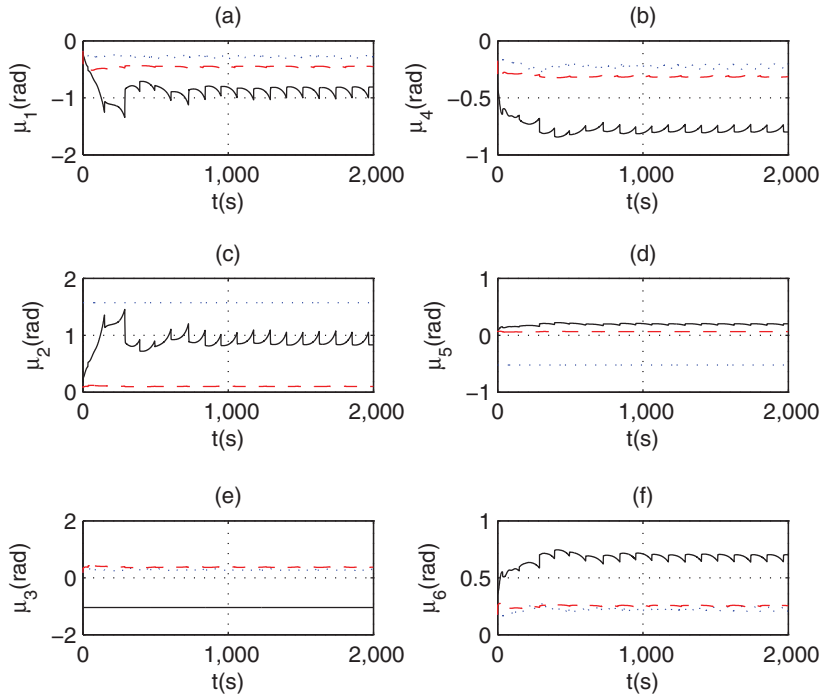

Figure 28. (Colour online) Vectored angles in trace tracking of failure cases.

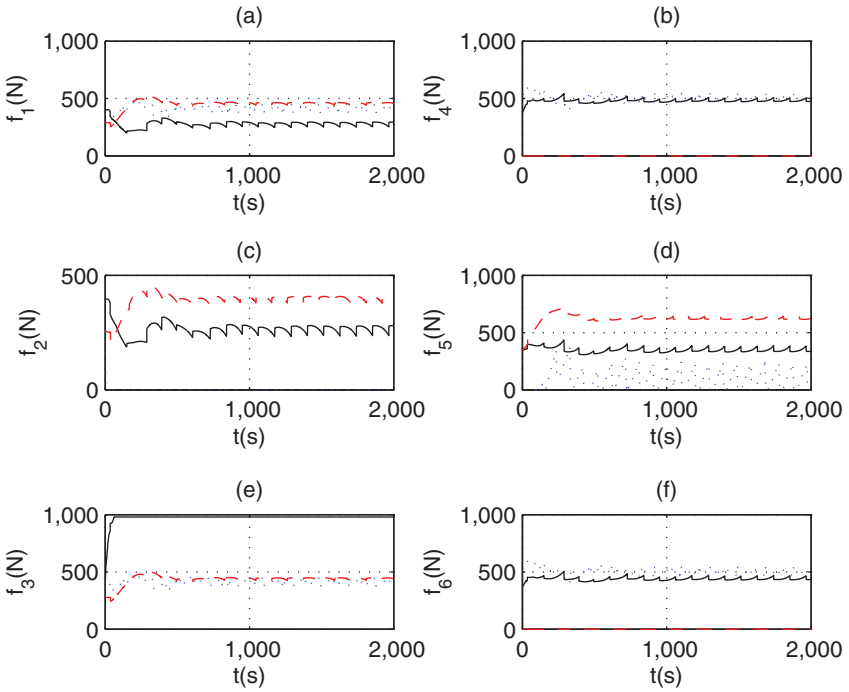

Figure 29. (Colour online) Thrusts in trace tracking of failure cases.

https://doi.org/10.1017/aer.2017.125 Published online by Cambridge University Press

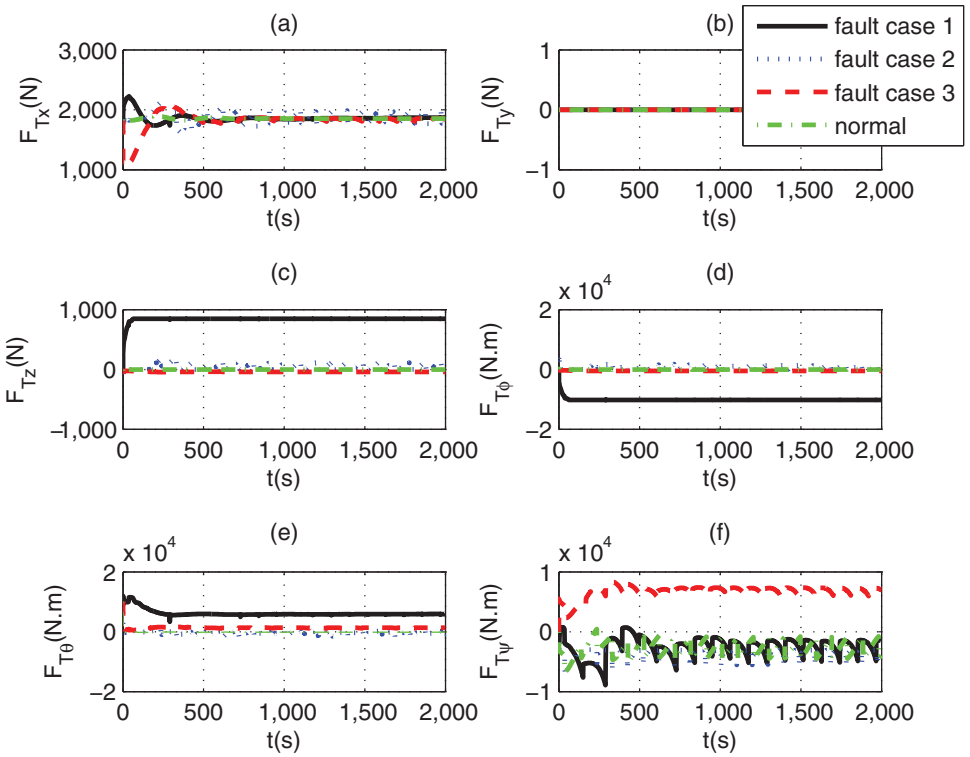

Figure 30. (Colour online) Control force allocation of propellers in trace tracking of failure cases.

4.2.2 Control force allocation of multi-propellers

With respect to the control force allocation of the propellers, it can be seen from Figs 25, 30 and 35, that in case of fault situations, the actuator allocation strategy tends to relocate the actuators to achieve the same control forces as in the normal situation shown in Figs 25(a) and 30(a) for forward force and in Fig. 35(e) for pitch moment.

In plenary motion of position control and trace tracking, there are some pitch and roll moments generated because of the asymmetric drive of fault propellers, so the roll and pitch disturbance moments occurred (in Fig. 25(d, e) and Fig. 30(d, e)), also because of the fault propeller 3 is stuck at -60°, there is altitude disturbance, so extra vertical force is generated (in Figs 25(c) and 30(c)).

For vertical motion of altitude control, in failure case 2, the stuck propeller 2 generated vertical force to assist altitude control as shown in Fig. 35(c), and there are coupling roll moment and yaw moment generated due to the asymmetrical drive of fault propellers (in Fig. 35(d, f)).

5.0 CONCLUSION

The composite control system of hybrid-heterogeneous actuators is designed for an airship. It includes guidance strategy, basic controller design, moment allocation and reconfigurable

https://doi.org/10.1017/aer.2017.125 Published online by Cambridge University Press

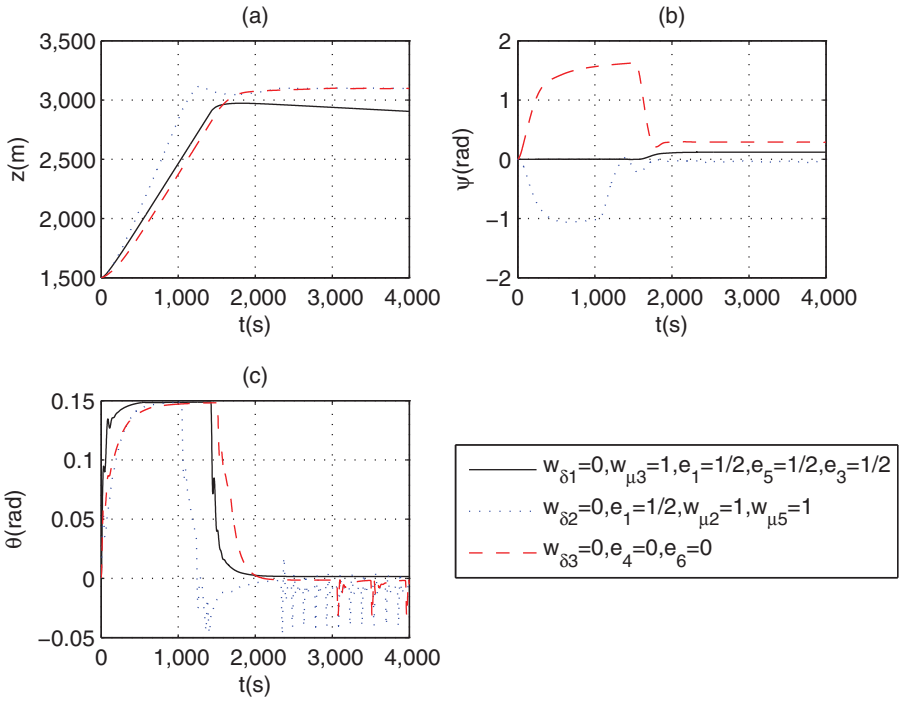

Figure 31. (Colour online) States in altitude control of failure cases.

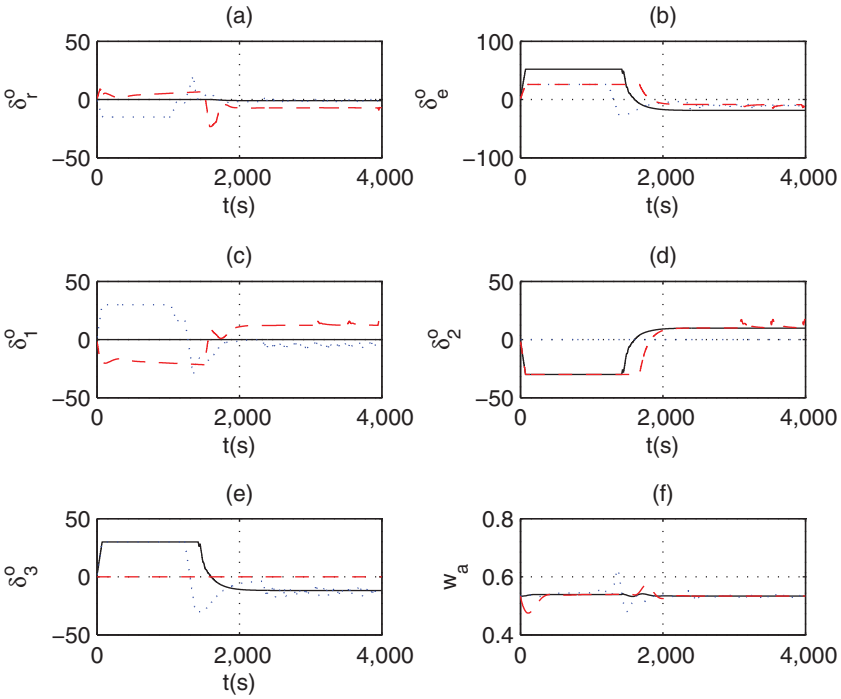

Figure 32. (Colour online) Aerodynamic deflections in altitude control of failure cases.

https://doi.org/10.1017/aer.2017.125 Published online by Cambridge University Press

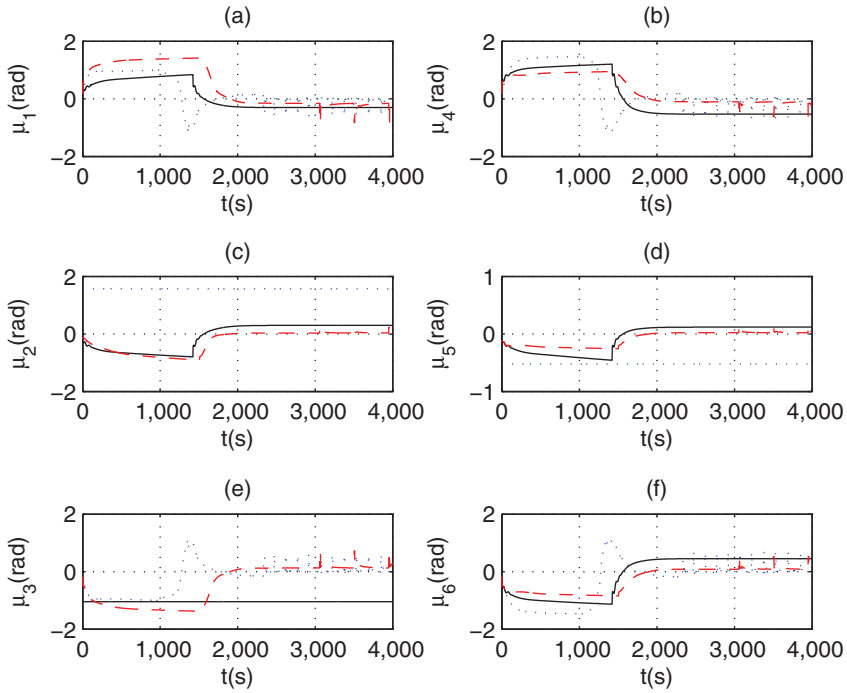

Figure 33. (Colour online) Vectored angles in altitude control of failure cases.

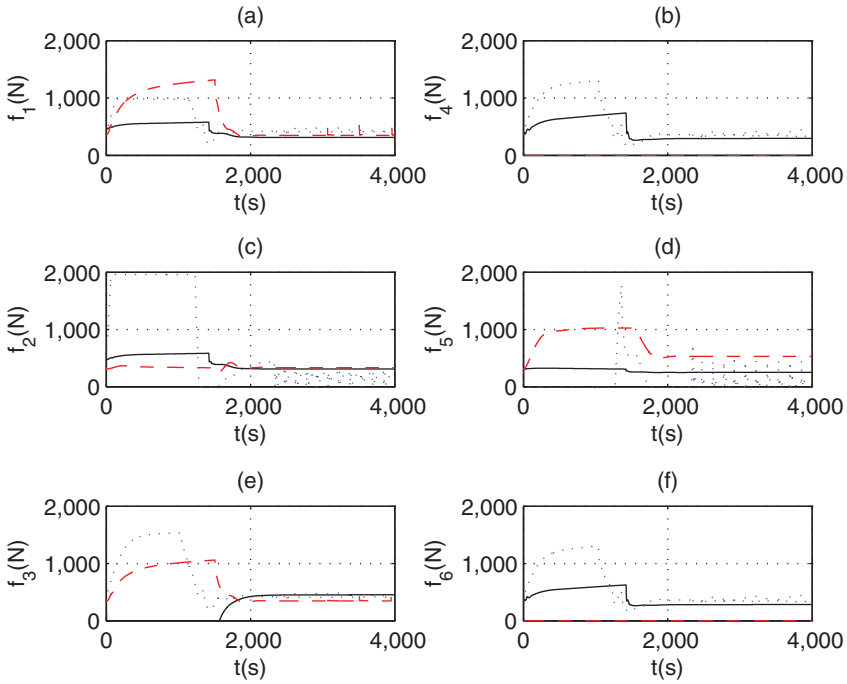

Figure 34. (Colour online) Thrusts in altitude control of failure cases.

https://doi.org/10.1017/aer.2017.125 Published online by Cambridge University Press

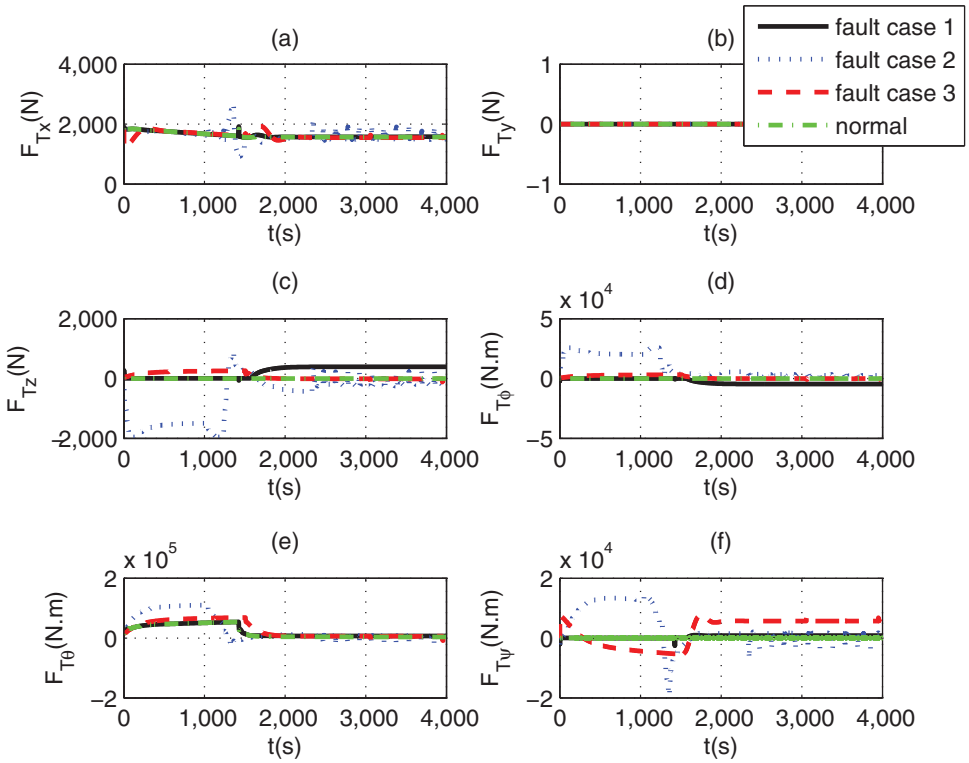

Figure 35. (Colour online) Control force allocation of propellers in altitude control.

actuator allocation. The novelty in the design of this control system are: (1) The indirect control force is introduced in the propeller model to guarantee existence of pseudo-inverse of the control coefficient matrix, thus this controller always has analytic solution, so it is easy to implement; (2) Three diagonal weight matrices are combined together to represent the all possible faults of vectored propeller, so this controller can be used on general situation. Using the mid-altitude airship as an example, the simulations of different control tasks are provided. The composite controller achieves a good distribution and reconfiguration among these heterogeneous actuators in case of failure, thereby enhancing the reliability of the control system.

ACKNOWLEDGEMENTS

This work was supported by National Science Foundation of China, no. 61733017 and no. 61175074.

REFERENCES

1. TAKASHI, K., NAKADATE, M. and OKUYAMA, M. On-going UAV R&D at JAXA's aviation program group- second report with emphasis on LTA flight control, 18th AIAA Lighter-Than-Air Systems Technology Conference, 4-7 May 2009, Seattle, Washington, US.

https://doi.org/10.1017/aer.2017.125 Published online by Cambridge University Press

2. AZINHEIRA, J.R., MOUTINHO, A. and CARVALHO, J.R. Lateral control of airship with uncertain dynamics using incremental nonlinear dynamics inversion, *IFAC-Papers On Line*, 2015, **48**(19), pp 69-74.
3. YANG, Y. and AN, Y. Neural network approximation-based nonsingular terminal sliding mode control for trajectory tracking of robotic airships, *Aerospace Science and Technology*, 2016, **54**, pp 192-197.
4. ZHENG, Z.W., CHEN, T, XU, M. and ZHU, M. Modelling and path-following control of a vector-driven stratospheric satellite, *Advances in Space Research*, 2016, **57**(9), pp 1901-1913.
5. LIU, Y., WU, Y.L. and HU, Y.M. Autonomous dynamics-modeling and feedback control for an airship, *Control Theory and Applications*, 2010, **27**(8), pp 991-997.
6. FAN, Y.H., YU, Y.F. and YAN, J. High altitude airship altitude control system design and simulation, *Science Technology and Engineering*, 2011, **11**(24), pp 5957-5961.
7. GUO, J.G. and ZHOU, J. Compound control system of stratospheric airship based on aircrew systems, *J Astronautics*, 2009, **30**(1), pp 225-230.
8. DI, X.G., HAN, F. and YAO, Y. Attitude control allocation strategy of high altitude airship based on synthetic performance optimization, *J Harbin Institute of Technology*, 2009, **16**(6), pp 746-750.
9. CHEN, L., ZHOU, G., YAN, X. J. and DUAN, D. P. Composite control strategy of stratospheric airships with moving masses, *J Aircr*, 2012, **49**(3), pp 794-800.
10. LIESK, T., NAHON, M. and BOULET, B. Design and experimental validation of a nonlinear low-level controller for an unmanned fin-less airship, *IEEE Transactions on Control Systems Technology*, 2013, **21**(1), pp 149-161.
11. BATTIPEDE, M., GILI, P. and LANDO, M. Ground station and flight simulator for a remotely-piloted non-conventional airship. AIAA Guidance, Navigation, and Control Conference and Exhibit, 2005, California, San Francisco, US.
12. ROOZ, N. and JOHNSON, E.N. Design and modeling of an airship station holding controller for low cost satellite operations, AIAA Guidance, Navigation, and Control Conference and Exhibit, 2005, San Francisco, California, US.
13. BERGE, S. P. and FOSSEN, T. I. Robust Control allocation of overactuated ships: experiments with a model ship, Proceedings of the 4th IFAC, Conference on Maneuvering and Control of Marine Craft, 1997, Brijuni, Croatia, pp 166-171.
14. JOHANSEN, T. A., FOSSEN, T. I. and BERGE, S. P. Constraint nonlinear control allocation with singularity avoidance using sequential quadratic programming, *IEEE Transactions on Control Systems Technology*, TCST-12, 2004, pp 211-216.
15. DURHAM, W. C. Constrained control allocation, *J Guidance, Control and Dynamics*, 1993, **16**(4), pp 717-725.
16. BORDIGNON, K.A. Constrained control allocation for systems with redundant control effectors, PhD thesis, 1996, Virginia Polytechnic Institute and State University, Blacksburg, Virginia, US.
17. BUFFINGTON, J. M. and ENNS, D. F. Lyapunov stability analysis of daisy chain control allocation, *J Guidance, Control, and Dynamics*, 1996, **19**(6), pp 1226-1230.
18. ENNS, D. Control allocation approaches, Proceedings of the AIAA Guidance, Navigation, and Control Conference and Exhibit, 1998, Reston, Virginia, US, pp 98-108.
19. LANE, S.H. and STENGEL, R.F. Flight control design using non-linear inverse dynamics, *Automatica*, 1988, **24**(4), pp 471-483.
20. ENNS, D., BUGAJSKI, D., HENDRICK, R. and STEIN, G. Dynamic inversion: an evolving methodology for flight control design, *Int J Control*, 1994, **59**(1), pp 71-91.
21. IKEDA, Y. and HOOD, M. An application of L1 optimization to control allocation, AIAA Guidance, Navigation, and Control Conference and Exhibit, August 2000, Denver, Colorado, US.
22. BODSON, M. Evaluation of optimization methods for control allocation. *J Guidance, Control and Dynamics*, 2002, **25**, pp 703-711.
23. REIMAN, S.E. and DILLON, C.H. Robust adaptive reconfigurable control for a hypersonic cruise vehicle, AIAA Guidance, Navigation, and Control Conference, 10-13 August 2009, Chicago, Illinois, AIAA 2009-6185.
24. DAVIDSON, J.B., LALLMAN, F.J. and BUNDICK, W.T. Integrated reconfigurable control allocation, AIAA Guidance, Navigation, and Control Conference and Exhibit, 2001, Montreal, Canada, AIAA 2001-4083.
25. WANG, X.L., FU, G.Y., DUAN, D.P. and SHAN, X.X. Experimental Investigations on aerodynamic characteristics of the ZHIYUAN-1 Airship, *J Aircr*, 2010, **47**(4), pp 1463-1469.

https://doi.org/10.1017/aer.2017.125 Published online by Cambridge University Press

26. ZHANG, M.H, DUAN, D.P. and CHEN, L. Turning mechanism and composite control of stratospheric airships, *J Zhejiang University, Science C*, 2012, **13**(11), pp 859-865.
27. CHEN, L. and DUAN, D. Attitude control of stratospheric airship with ballonets and elevator, Proceedings of the 32nd Chinese Control Conference, 26-28 July 2013, Xi'an, China, pp 4255-4258.

https://doi.org/10.1017/aer.2017.125 Published online by Cambridge University Press